TITLE:

Investigation of combustion noise generated by an open lean-premixed H/air low-swirl flame using the hybrid LES/APE-RF framework

AUTHOR(S):

Pillai, Abhishek Lakshman; Inoue, Shimpei; Shoji, Takeshi; Tachibana, Shigeru; Yokomori, Takeshi; Kurose, Ryoichi

Contents lists available at ScienceDirect

Combustion and Flame

journal homepage: www.elsevier.com/locate/combustflame
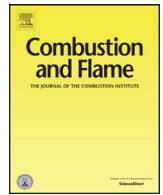
Investigation of combustion noise generated by an open lean-premixed H$_2$/air low-swirl flame using the hybrid LES/APE-RF framework

Abhishek Lakshman Pillai [a,*], Shimpei Inoue [a], Takeshi Shoji [b], Shigeru Tachibana [b], Takeshi Yokomori [c], Ryoichi Kurose [a]

[a] Department of Mechanical Engineering and Science, Kyoto University, Kyoto daigaku-Katsura, Nishikyo-ku, Kyoto 615–540, Japan
[b] Aviation Technology Directorate, Japan Aerospace Exploration Agency, Chofu, Tokyo 182-8522, Japan
[c] Department of Mechanical Engineering, Keio University, Yokohama, Kanagawa 223-8522, Japan

ARTICLE INFO

ABSTRACT

An open lean-premixed hydrogen/air low-swirl (LPHALS) turbulent flame exhibiting a pronounced peak in its combustion noise spectra, is investigated numerically using a hybrid Computational Fluid Dynamics/Computational Aero-Acoustics (CFD/CAA) framework. Under this framework, the reacting flow-field of the flame is computed via Large-Eddy Simulation (LES), while the direct combustion noise it produces is captured by solving the Acoustic Perturbation Equations for Reacting Flows (APE-RF). Flame configuration and simulation conditions correspond to those of an experimental study on an open lean-premixed H$_2$/air flame stabilized using a Low-Swirl Burner (LSB). LES results are validated against experimental data. The CAA simulation is able to predict a pronounced sharp peak in the computed combustion noise spectra, similar to one of the two characteristic peaks observed in the measured combustion noise spectra. Frequency of this spectral peak predicted by the CAA simulation is 840 Hz, which is close to that of the higher frequency secondary spectral peak at 940 Hz measured in the experiment. Upon examining the hybrid LES/APE-RF results, the noise generation mechanism at 840 Hz is found to be the intense local heat release rate fluctuations, caused by strong interaction between the flame and the periodically generated vortical flow structures in the shear layers, downstream of the LSB exit. Additionally, analysis of the spectral content and directivity of the noise generated by different acoustic source terms is performed, in order to investigate their impact on the radiated acoustic field, and hence the characteristics of direct combustion noise produced by the open LPHALS flame.

1. Introduction

Lean-premixed combustion has been garnering attention in research efforts over the past decade, to regulate the ever-increasing emissions of greenhouse gases (e.g., CO$_2$ and N$_2$O) and NOx, and to improve the thermal efficiencies of combustors [1]. However, lean-premixed combustion has been found to be inherently unsteady [2,3], and can thereby enhance combustion noise emissions. Pressure perturbations generated by such unstable turbulent combustion may couple with the unsteady heat release in turbulent confined flames (e.g., inside a gas turbine combustor), if a feed-back is established between said pressure perturbations and the flame, thus, triggering thermo-acoustic instabilities [2,4,5]. Hence, combustion noise reduction is considered to be an important issue not just in terms of compliance with regulatory noise emission standards (to avoid adverse effects on public health and quality of life), but also for preventing damage to gas turbine combustors from thermo-acoustic instabilities, and reducing their maintenance costs.

Although noise generation from premixed [6–9] and non-premixed [10–13] flames has been an actively pursued research topic, there are still open questions in this field of research, especially pertaining to the differences in the combustion noise characteristics between premixed and non-premixed flames, such as compactness, scaling relations, and spectral content and directivity of the radiated acoustic field. Another open research issue of

particular importance to gas turbine combustors that is not yet fully understood is the relative contributions of the two important noise generation mechanisms comprising engine-core noise, viz. the direct and indirect combustion noise, to the overall engine-core noise emission [14]. Direct combustion noise refers to the acoustic perturbations arising from the unsteady heat release and is perceived as the unsteady volumetric expansion and contraction of the reacting gas mixture caused by the heat release fluctuations [6]. It is a characteristic of open turbulent flames. On the other hand, indirect combustion noise is generated by the acceleration of entropy, vorticity, and compositional inhomogeneities when they convect from the combustor to the turbine stages and nozzle situated downstream of the combustor exit in a gas turbine [14–17]. While direct combustion noise generation from open turbulent premixed, non-premixed, and partially premixed flames is of interest at the fundamental level, the generation of indirect combustion noise from confined flames in gas turbines has also been a subject of active research [14,17–19]. An elaborate discussion on the aforementioned open research issues can be found in the review article by Ihme [14]. Investigations of direct combustion noise with sharp spectral peaks emitted by unconfined lean-premixed flames are few. One example is the experimental interrogation of self-induced combustion oscillations of laminar premixed CH4/air flames conducted by Schuller et al. [20]. In their study, it was shown that self-induced instabilities can occur in open flames (and not just confined flames), and the measured direct combustion noise spectra of those laminar premixed flames (with different equivalence ratios of ϕ = 1.13, 1.20 and 1.28) comprised clear pronounced peaks. However, in their study [20], only the fuel-rich laminar premixed flames were susceptible to self-induced instabilities. In a more recent experimental investigation performed by Shoji et al. [21] at JAXA, open lean-premixed H_2/air low-swirl (LPHALS) turbulent flames were considered. It was found that the combustion noise spectra of these unconfined flames are characterized by sharp double peaks for equivalence ratios as low as ϕ = 0.45. Hence, they [21] elucidated the physical mechanisms underlying the generation of pronounced double peaks in the direct combustion noise spectra of open LPHALS flames.

In terms of numerical studies, although Direct Numerical Simulation (DNS) has been applied to investigate direct combustion noise [22], the hybrid CFD/CAA framework has gained popularity in recent years. In particular, the hybrid LES/APE-RF framework has been applied to analyze direct combustion noise from open turbulent premixed [23,24] and diffusion [25] jet flames, and a hybrid DNS/APE-RF approach has also been applied to an open spray jet flame [26] to analyze its combustion noise. The hybrid CFD/CAA framework has also been employed in the investigation of indirect combustion noise in a realistic gas turbine combustor by Shao et al. [18,19]. They developed a hybrid simulation framework that combines LES for computing the unsteady turbulent reacting flow field inside the combustor with a linearized Euler solver which describes the generation and transmission of noise through the downstream nozzle (as the solution to the linearized Euler equations). These studies [18,19] revealed that the contribution of indirect combustion noise to the overall noise emission is appreciable at low frequencies and that this contribution of the indirect combustion noise depends strongly on the engine's operating conditions. In another study, Pausch et al. [27] used the hybrid LES/APE-RF approach to investigate the acoustic sources of a confined premixed methane-air high-swirl flame subjected to a self-excited thermoacoustic instability inside a model swirl combustor without a nozzle downstream of the combustor. But their study proved that the hybrid LES/APE-RF framework (which is also employed in the present work) has the potential to be applied for investigating the indirect combustion noise from confined flames in gas turbine combustors, with the appropriate formulations of the acoustic

source terms and the Acoustic Perturbation Equations (APE), i.e., the APE-4 system used in Pausch et al.'s studies [24,27].

However, many of these previous numerical studies [22–26] primarily focus on hydrocarbon-fueled jet flames with relatively simple configurations, and unconfined lean-premixed H_2/air swirling flames emitting direct combustion noise with sharp spectral peaks, have not yet been examined using the hybrid LES/APE-RF framework. Furthermore, to attain the goal of net zero CO_2 emissions and become carbon-neutral by 2050, the dependence on hydrocarbon fuels needs to be reduced. Thus, the commercial use of hydrogen, which is a carbon-free clean fuel, is considered to be an excellent and sustainable alternative to conventional hydrocarbon fuels used in gas turbines. Therefore, the objective of our study is to use the hybrid LES/APE-RF framework for simulating an open LPHALS turbulent flame and its acoustic field, in order to obtain insight into the mechanism resulting in the pronounced peak in the flame's direct combustion noise spectra, and to investigate the characteristics of direct combustion noise radiated from it. Specifically, the influence of different acoustic source terms on the radiated acoustic field is investigated, by analysing the spectral content and directivity of the noise generated by them. To the best of the authors' knowledge, this is the first study to numerically investigate this kind of combustion noise from an open LPHALS flame, using the hybrid LES/APE-RF framework.

2. Hybrid LES/APE-RF framework

The hybrid LES/APE-RF framework couples the reacting flow-field's simulation (performed using LES) with the acoustic field's simulation (i.e., CAA), and hence comprises two steps. In the first step, LES of the open LPHALS flame is performed, and in the second step, the CAA simulation is performed to predict the acoustic field generated by this flame. In low Mach number reacting flows, the characteristic fluid-dynamic length scales are typically an order of magnitude smaller than the characteristic acoustic length scales. The hybrid LES/APE-RF framework leverages this large disparity between the characteristic fluid-dynamic and acoustic length scales, and separates the computations of the reacting flow field and the acoustic field.

2.1. Large-Eddy Simulation

In this study, the Flamelet Generated Manifold (FGM) approach [28] is employed as the combustion model. Hence, the Favre-filtered form of the conservation equations of mixture fraction $\widetilde{Z}$ and reaction progress variable $\widetilde{C}$ (defined as the sum of mass fractions of H_2O and OH, i.e., $\widetilde{C} = \widetilde{Y}_{H_2O} + \widetilde{Y}_{OH}$) are solved along with those of mass and momentum, and these governing equations are given as:

$$\frac{\partial \overline{\rho}}{\partial t} + \nabla \cdot (\overline{\rho}\widetilde{\boldsymbol{u}}) = 0 \tag{1}$$

$$\frac{\partial \overline{\rho}\widetilde{\boldsymbol{u}}}{\partial t} + \nabla \cdot (\overline{\rho}\widetilde{\boldsymbol{u}}\widetilde{\boldsymbol{u}}) = -\nabla \overline{p} + \nabla \cdot \overline{\boldsymbol{\tau}} - \nabla \cdot \overline{\boldsymbol{\tau}}^{sgs} \tag{2}$$

$$\frac{\partial \overline{\rho}\widetilde{Z}}{\partial t} + \nabla \cdot (\overline{\rho}\widetilde{Z}\widetilde{\boldsymbol{u}}) = \nabla \cdot (\overline{\rho}\widetilde{D}_Z\nabla\widetilde{Z}) - \nabla \cdot \boldsymbol{J}_Z^{sgs} \tag{3}$$

$$\frac{\partial \overline{\rho}\widetilde{C}}{\partial t} + \nabla \cdot (\overline{\rho}\widetilde{C}\widetilde{\boldsymbol{u}}) = \nabla \cdot (\overline{\rho}\widetilde{D}_C\nabla\widetilde{C}) - \nabla \cdot \boldsymbol{J}_C^{sgs} + \overline{\rho}\widetilde{\omega}_C \tag{4}$$

In the above equations, the overbar $^-$ indicates spatial filtering of a physical quantity, while the tilde $^\sim$ represents Favre filtering. Additionally, $\widetilde{\boldsymbol{u}}$ is the velocity vector, $\overline{\rho}$ is the density, $\overline{p}$ is the pressure, and $\overline{\boldsymbol{\tau}}$ is the resolved viscous stress tensor. The unresolved or subgrid-scale (SGS) stress tensor $\overline{\boldsymbol{\tau}}^{sgs}$, given as $\overline{\boldsymbol{\tau}}^{sgs} = \overline{\rho}(\widetilde{\boldsymbol{u}\boldsymbol{u}} - \widetilde{\boldsymbol{u}}\widetilde{\boldsymbol{u}})$ is

computed using a Dynamic Smagorinsky model [29,30] based on an eddy viscosity assumption. $\widetilde{D}_Z$ and $\widetilde{D}_C$ are the diffusion coefficients of the mixture fraction Z and the reaction progress variable C, respectively; they are defined as $\widetilde{D}_Z = \widetilde{D}_C = \lambda/(\rho c_p)$ under the unity Lewis number assumption ($Le = 1.0$), where λ is the thermal conductivity and c_p is the specific heat capacity at constant pressure. Moreover, $\boldsymbol{J}_\psi^{sgs} = \overline{\rho \boldsymbol{u} \psi} - \overline{\rho} \widetilde{\boldsymbol{u}} \widetilde{\psi}$ (where, $\psi = [Z, C]$) denotes the residual subgrid scalar flux in the transport equations of $\widetilde{Z}$ and $\widetilde{C}$, and is modelled based on the eddy diffusivity ansatz as follows:

$$\boldsymbol{J}_\psi^{sgs} = -\overline{\rho}\alpha_t \nabla \widetilde{\psi} \tag{5}$$

where, α_t represents the turbulent eddy diffusivity and is calculated as $\alpha_t = \mu_t/(\overline{\rho}Sc_t)$. Here, Sc_t is the turbulent Schmidt number and μ_t is the turbulent viscosity evaluated using a dynamic procedure [30]. In the FGM approach, thermochemical properties such as $\widetilde{\dot{\omega}}_C$ which is the reaction rate of progress variable C, temperature T, and the mass fractions of various chemical species $\widetilde{Y}_k$ at each grid point in the computational domain, are extracted from a pre-tabulated database called the flamelet library (explained later). For extracting these thermochemical properties (i.e., $\widetilde{\dot{\omega}}_C$, T and $\widetilde{Y}_k$), a reduced set of control variables, viz. $\widetilde{Z}$, $\widetilde{C}$, and $\widetilde{C''^2}$ (which represents the subgrid Favre variance of reaction progress variable C) [31] are adopted. In this study, $\widetilde{C''^2}$ is evaluated using the following algebraic gradient model:

$$\widetilde{C''^2} = \alpha_C \Delta^2 |\nabla \widetilde{C}|^2 \tag{6}$$

where Δ is the filter width and α_C is the model constant set to 0.1 based on a previous study [32].

2.1.1. Combustion model: Flamelet Generated Manifold

Combustion of hydrogen is modelled in the LES via the Flamelet Generated Manifold (FGM) approach [28]. In this approach, the premixed flamelet library is constructed by solving the flamelet equations for 1D freely propagating laminar premixed flame. The 1D laminar flame computations are performed for several values of equivalence ratio ϕ in the range of $0.27 \leq \phi \leq 1.0$ using the FlameMaster code [37]. In order to select a suitable reaction mechanism for constructing the premixed flamelet library, two detailed chemical kinetic mechanisms are employed in the 1D laminar flame computations and their performance is evaluated. The first detailed reaction mechanism to be tested, is the one proposed by Miller and Bowman [33] which comprises 20 chemical species and 73 reactions, and the latter is the one proposed by Ó Conaire et al. [34] which comprises 9 chemical species and 20 reactions. Conditions at which the 1D laminar flame computations are performed, are the same as those in the experiment conducted by Shoji et al. [21], i.e., pressure $p = 1$ atm and unburnt premixed gas temperature $T_u = 300$ K. The laminar flame speeds S_L obtained from the 1D premixed flame computations employing both the aforementioned detailed reaction mechanisms, are compared with the measurements of Egolfopoulos and Law [35] and Lamoureux et al. [36] in Fig. 1. It is evident that S_L predicted using Miller and Bowman's detailed reaction mechanism [33] agrees favourably with the experimental data and outperforms Ó Conaire et al.'s mechanism [34]. Especially for $\phi = 0.45$, which is the equivalence ratio of the LPHALS flame targeted in this study, Ó Conaire et al.'s mechanism [34] underestimates the laminar flame speed S_L. Hence, the detailed chemical kinetic mechanism of Miller and Bowman [33] is adopted for generating the premixed flamelet library.

2.2. Computational Aero-Acoustics simulation

To predict combustion noise emitted by the open LPHALS flame, the system of Acoustic Perturbation Equations extended to Reacting Flows (APE-RF) [25], which is capable of simulating acoustic
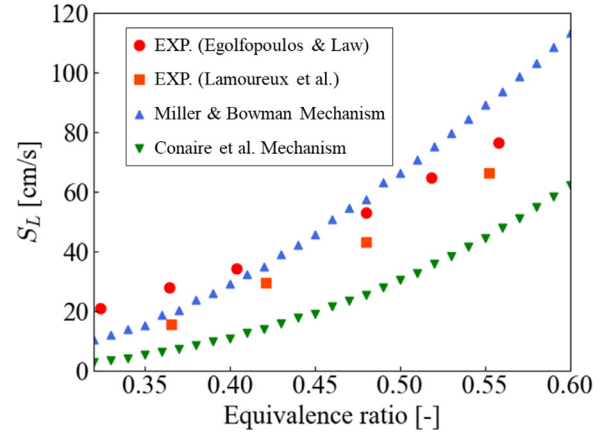

Fig. 1. Comparison of laminar flame speeds S_L predicted using Miller and Bowman's mechanism [33] and Ó Conaire et al.'s mechanism [34] with experimental measurements [35,36], as a function of equivalence ratio ϕ at pressure $p = 1$ atm and unburnt gas temperature $T_u = 300$ K.

wave propagation in arbitrary mean flows while taking convection and refraction effects into consideration, is solved in the Computational Aero-Acoustics (CAA) simulation. The APE-RF comprise the following equations for perturbation density ρ', perturbation velocity $\boldsymbol{u}'$ and perturbation pressure p' [25,38]:

$$\frac{\partial \rho'}{\partial t} + \nabla \cdot \left(\rho' \hat{\boldsymbol{u}} + \hat{\rho} \boldsymbol{u}' \right) = q_{c,rf} \tag{7}$$

$$\frac{\partial \boldsymbol{u}'}{\partial t} + \nabla \left(\hat{\boldsymbol{u}} \cdot \boldsymbol{u}' \right) + \nabla \left(\frac{p'}{\hat{\rho}} \right) = \boldsymbol{q}_{m,rf} \tag{8}$$

$$\frac{\partial p'}{\partial t} - \hat{c}^2 \frac{\partial \rho'}{\partial t} = q_{e,rf} \tag{9}$$

wherein, the dependent variables in Eqs. (7)–(9), viz. density ρ, velocity $\boldsymbol{u}$ and pressure p are decomposed into temporal mean (denoted by a hat ˆ, i.e., $\hat{\rho}$, $\hat{\boldsymbol{u}}$, $\hat{p}$), and fluctuating (denoted by a prime $'$, i.e., ρ', $\boldsymbol{u}'$, p') components. $\hat{c}$ is the mean speed of sound, while $q_{c,rf}$, $\boldsymbol{q}_{m,rf}$ and $q_{e,rf}$ (quantities appearing on the right-hand side of the APE-RF) represent the source terms responsible for the excitation of acoustic waves, and are expressed as [25]:

$$q_{c,rf} = -\nabla \cdot \left(\rho' \boldsymbol{u}' \right)' \tag{10}$$

$$\boldsymbol{q}_{m,rf} = -(\boldsymbol{\omega} \times \boldsymbol{u})' - \nabla k' + \nabla \left(\frac{p'}{\hat{\rho}} \right) - \left(\frac{\nabla p}{\rho} \right)' + \left(\frac{\nabla \cdot \boldsymbol{\tau}}{\rho} \right)' \tag{11}$$

$$q_{e,rf} = -\hat{c}^2 \left[\left(\frac{\hat{\rho}}{\rho} + \frac{p - \hat{p}}{\rho \hat{c}^2} \right) \frac{D\rho}{Dt} - \nabla \cdot (\boldsymbol{u} \rho_e) - \boldsymbol{u} \cdot \nabla \hat{\rho} - \frac{D}{Dt} \left(\frac{p - \hat{p}}{\hat{c}^2} \right) \right] \tag{12}$$

where $\boldsymbol{\omega}$ is the vorticity vector (i.e., $\boldsymbol{\omega} = \nabla \times \boldsymbol{u}$), k is the turbulent kinetic energy, $\boldsymbol{\tau}$ is the viscous stress tensor, and ρ_e is the excess density [39] defined as:

$$\rho_e = (\rho - \hat{\rho}) - \frac{(p - \hat{p})}{\hat{c}^2} \tag{13}$$

The acoustic source terms $q_{c,rf}$, $\boldsymbol{q}_{m,rf}$ and $q_{e,rf}$, and the mean flow quantities, viz. mean density $\hat{\rho}$, mean velocity $\hat{\boldsymbol{u}}$ and mean speed of sound $\hat{c}$ required for solving the system of APE-RF in Eqs. (7)-(9), are computed from the solution of the LES of the open LPHALS flame performed in the first step. These quantities are then mapped from the LES grid onto the CAA grid using a trilinear algorithm [25,26]. The acoustic source term $q_{e,rf}$ of the pressure-density relation in Eq. (9), contains various source mechanisms
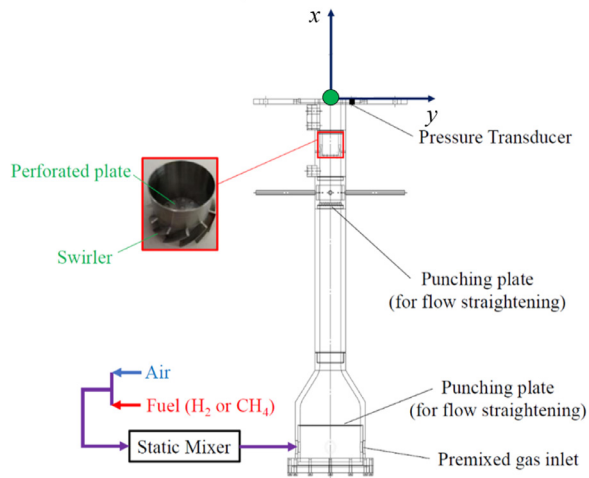
Fig. 2. Schematic of the Low-Swirl Burner used in the experimental study of Shoji et al. [21].

Fig. 3. Schematic of computational domain and conditions for LES.

that excite acoustic waves in combustion noise. In Eq. (12) for the source term $q_{e,rf}$, the substantial time derivative of density $D\rho/Dt$ in the first term on the right-hand side, implicitly describes the effects of heat release rate per unit volume, volumetric expansion caused by non-isomolar combustion, species diffusion, heat diffusion and viscous effects [25,38]. Thus, the acoustic source term $q_{e,rf}$ contains one of the dominant source mechanisms of combustion noise, i.e., the unsteady heat release. Derivation of the APE-RF system is presented in Bui et al. [40], and a detailed discussion of the acoustic source terms and the various source mechanisms contained in them is available in [25,38,40].

2.3. Computational configurations and solution algorithms

Computational configuration and conditions of the LES are described first. A schematic of the Low-Swirl Burner (LSB) used in the experiments of Shoji et al. [21] to measure the open LPHALS turbulent flame's flow field and direct combustion noise characteristics, is depicted in Fig. 2. The LSB has an inner exit diameter of $d = 35$ mm. A swirler assembly comprising an annular vane swirler and a central channel, is recessed from the burner exit plane in the upstream direction at a distance of 43 mm. The annular swirler is equipped with 12 curved blades, each inclined at $37°$ with respect to the burner axis. A perforated screen with a diameter of 25 mm was fitted to the bottom of the vane swirler to enable a portion of the reactants to bypass the swirl annulus, and thus remain unswirled. This perforated screen comprises 19 holes of 3.6 mm diameter each and has a blockage ratio of 66.2% on the central channel. The geometric swirl number of the annular vane swirler is 0.39. Further details of the experimental configuration (i.e., the LSB apparatus and the measurement techniques used) are discussed in Shoji et al. [21], and are not repeated here for the sake of brevity. Our preliminary estimates showed that approximately 0.8 Billion grid points would be needed for the LES, if this complex LSB geometry comprising the annular vane swirler assembly and perforated screens is to be incorporated inside the LES's computational domain.

However, owing to limited computational resources and to keep computational costs realizable, the computational domain of the present LES does not include this complex LSB geometry situated upstream of the burner exit as in the experiment. Instead, the LES is performed only in the region downstream of the burner exit starting from the burner exit, as illustrated in Fig. 3 which shows a schematic of the LES's computational domain along with the in-
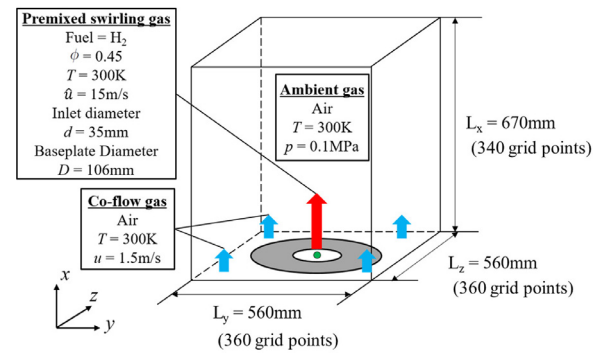
flow conditions. Similar to Shoji et al.'s experiment [21], unburned swirling H_2/air premixed gas at an equivalence ratio of $\phi = 0.45$ and temperature of 300 K, flows out of the burner exit into air at 300 K and standard atmospheric pressure. The bulk velocity of the gas mixture at the burner exit is 15 m/s. The LES domain measures 670 mm × 560 mm × 560 mm in the x-, y- and z-directions, respectively. Origin of the LES domain is the point on the burner axis at the burner exit plane, denoted by the green dot in Fig. 3. LES is performed on a non-uniform staggered Cartesian grid featuring 340 grid points in the streamwise x-direction, and 360 grid points each in the y- and z-directions. Minimum grid spacing used in the LES grid is $\Delta x = \Delta y = \Delta z = 300$ μm. Burner exit diameter is $d = 35$ mm, and the annular grey patch surrounding the burner exit (see the inflow plane in Fig. 3) represents a solid metal baseplate that was present in the actual LSB setup of the experiment [21], with an outer diameter of 106 mm.

At the burner exit plane (i.e., at $x = 0$ mm) of the present LES, radial profiles of mean axial and radial velocity components and radial profiles of their corresponding RMS fluctuations measured at the burner exit in the experiment, are imposed as inflow velocity boundary conditions. Tangential velocity profiles were not measured in the experiment, hence a LES considering the full LSB geometry with the same governing equations, turbulence and combustion models described in Section 2.1, was performed using an unstructured commercial LES solver: FrontFlow/Red, which has been extended by Kyoto University, CRIEPI and NuFD (Numerical Flow Designing, Co., Ltd.), referred to as FFR-Comb [31,41,42]. The sole objective of performing this extremely expensive LES with FFR-Comb, was to obtain the radial profiles of mean tangential velocity and its RMS fluctuation at the burner exit, so that they can also be imposed as inflow boundary conditions in the present LES (performed in the computational domain depicted in Fig. 3), and ensure that the low-swirl flow is reproduced by the LES. Figure 4(a) shows the radial profiles of the mean axial, radial and tangential velocity components, and Fig. 4(b) shows the radial profiles of their corresponding RMS fluctuations (i.e., standard deviations), which are imposed as inflow velocity boundary conditions at the burner exit in the LES. Additionally, transient turbulent velocity fluctuations generated using a digital filter based technique [43,44] are superimposed on the mean velocity profiles shown in Fig. 4(a) at the burner exit. The radial profiles of RMS fluctuations of the velocity components depicted in Fig. 4(b) are fed as input data to the digital filter based artificial turbulence generator [43,44]. Outflow boundary conditions are applied at the upper $y − z$ plane at $x = 670$ mm (outlet of the LES domain) as well as the lateral $x − y$ and $x − z$ boundaries (see Fig. 3), meaning the pressure is fixed at 1 atm and the Neumann condition is imposed on the velocity. No-slip velocity boundary condition is applied on the solid base-plate's surface (denoted by the annular grey region
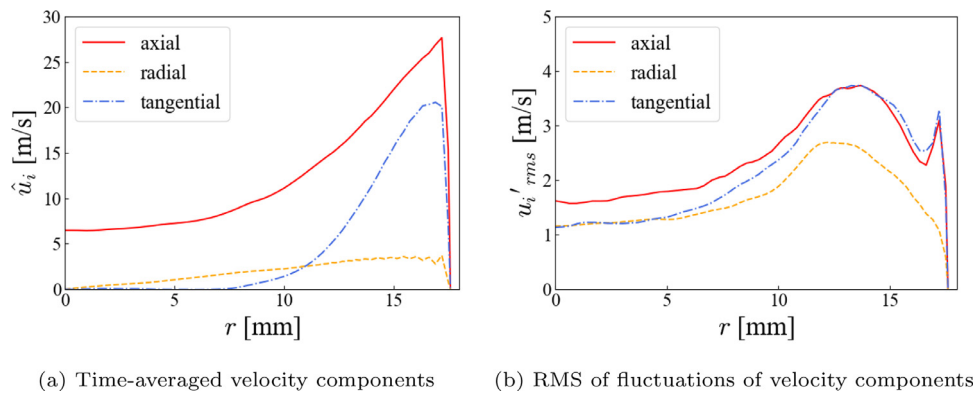
(a) Time-averaged velocity components

(b) RMS of fluctuations of velocity components

Fig. 4. Radial profiles of (a) time-averaged axial, radial and tangential velocity components, and (b) RMS of fluctuations of these velocity components, at the burner exit plane $x = 0$ mm.
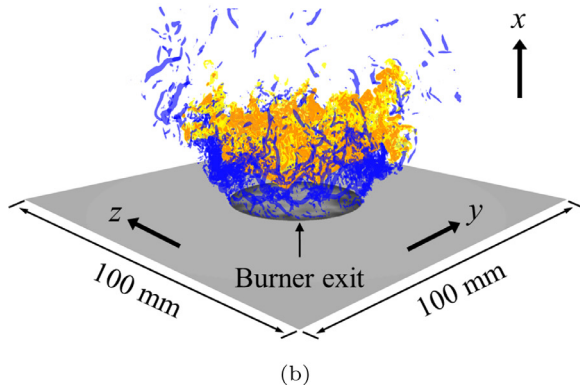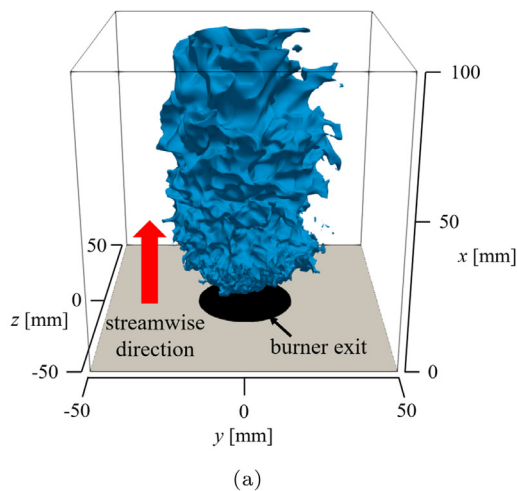

(a)

(b)

Fig. 5. Instantaneous distributions of (a) iso-surface of temperature at 1500 K (colored in blue), above the $y − z$ plane (i.e., the burner exit plane $x = 0$ mm, coloured in grey) with the burner exit represented by the black elliptical patch, and (b) iso-surfaces of heat release rate (coloured in yellow = 3×10^9 W/m^3 and orange = 4×10^9 W/m^3) and the second invariant of the velocity gradient tensor Q_2 (coloured in blue for $Q_2 > 0$). (For interpretation of the references to colour in this figure legend, the reader is referred to the web version of this article.)

surrounding the burner exit), which is assumed to be an adiabatic wall.

Next, the computational configuration and conditions of the CAA simulation are explained. The CAA domain is a cube with an edge length of 820 mm, and its extent in the respective Cartesian coordinate directions is in the range of: -75 mm $\leq x \leq$ 745 mm, -410 mm $\leq y \leq$ 410 mm, and -410 mm $\leq z \leq$ 410 mm. Thus, the

Table 1
CAA simulation cases performed in this study (◯: Acoustic source term is included in the CAA simulation case; ✕: Acoustic source term is excluded from the CAA simulation case).

CAA simulation cases	case1	case2	case3
Continuity source term, $q_{c,rf}$	◯	✕	✕
Momentum source term, $\boldsymbol{q}_{m,rf}$	◯	✕	◯
Energy source term, $q_{e,rf}$	◯	◯	✕

CAA domain is larger than the LES domain and completely encompasses the LES domain. CAA simulation is performed on a non-uniform Cartesian grid consisting of 300 × 320 × 320 grid points in the x-, y- and z-directions, respectively. Origin of the CAA domain is the same as that of the LES domain (green point on the burner axis at the burner exit plane, see Fig. 3). The non-reflective radiation boundary conditions [45] are applied at the far-field boundaries of the CAA domain, because the APE-RF system does not describe the convection of vorticity and entropy modes [25,38]. Minimum grid spacing used in the CAA grid is $\Delta x = \Delta y = \Delta z = 900$ μm, which is thrice that of the LES grid. Therefore, in this hybrid LES/APE-RF framework, LES of the turbulent combustion field is performed in a relatively smaller computational domain with fine grid, while the CAA simulation is performed on a coarser grid covering a larger acoustic domain, in order to capture acoustic wave propagation all the way into the far-field. By restricting the LES to a smaller computational domain containing the acoustic source region, the computational cost of LES can be reduced. Hence, the hybrid LES/APE-RF framework is computationally more efficient and less expensive than performing a large-scale LES alone of the open LPHALS flame using a large computational domain (same size as the CAA domain) with finer grid.

The hybrid LES/APE-RF simulation is performed using an in-house hybrid CFD/CAA code called FK^3-CAA [26], which is a combination of our in-house thermal flow analysis code FK^3 [46] and our CAA solver [26]. The FK^3 code, which is used for the LES, employs a pressure-based semi-implicit solver for compressible flows, whose algorithm comprises a fractional-step method [47]. In the LES, a 6th order accurate finite difference scheme [48] is used for the spatial discretization of the convective term in the momentum equation, i.e., Eq. (2). A 5th order Weighted Essentially Non-Oscillatory (WENO) scheme [49] is used for the spatial discretization of the convective terms in the governing equations of the scalar quantities, i.e., Eqs. (1), (3) and (4). A 3rd order explicit Total Variation Diminishing (TVD) Runge-Kutta scheme is employed for time integration of the convective terms in Eqs. (1)-(4). Thermodynamic properties and transport coefficients taking temperature
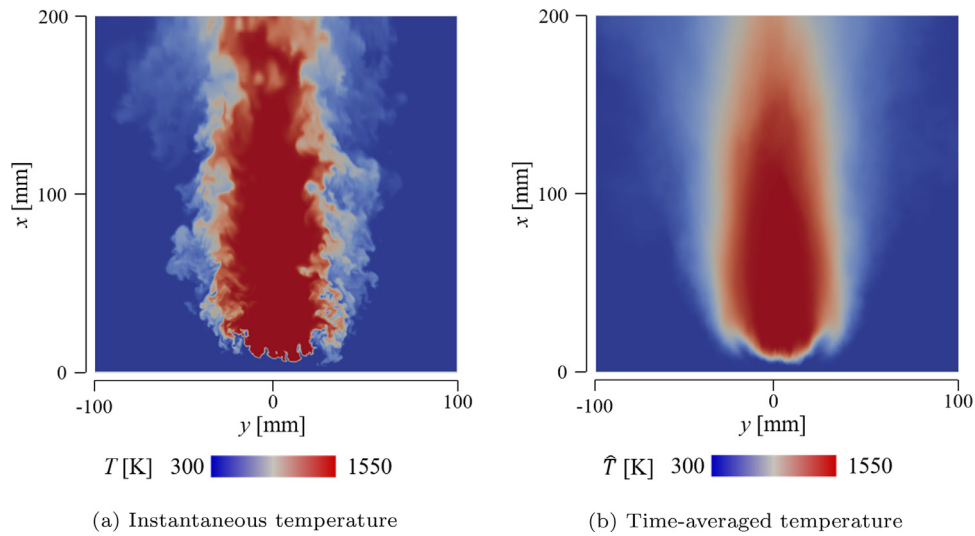
(a) Instantaneous temperature   (b) Time-averaged temperature

Fig. 6. Distributions of (a) instantaneous and (b) time-averaged temperature in the central $x - y$ plane ($z = 0$ mm) obtained from LES.
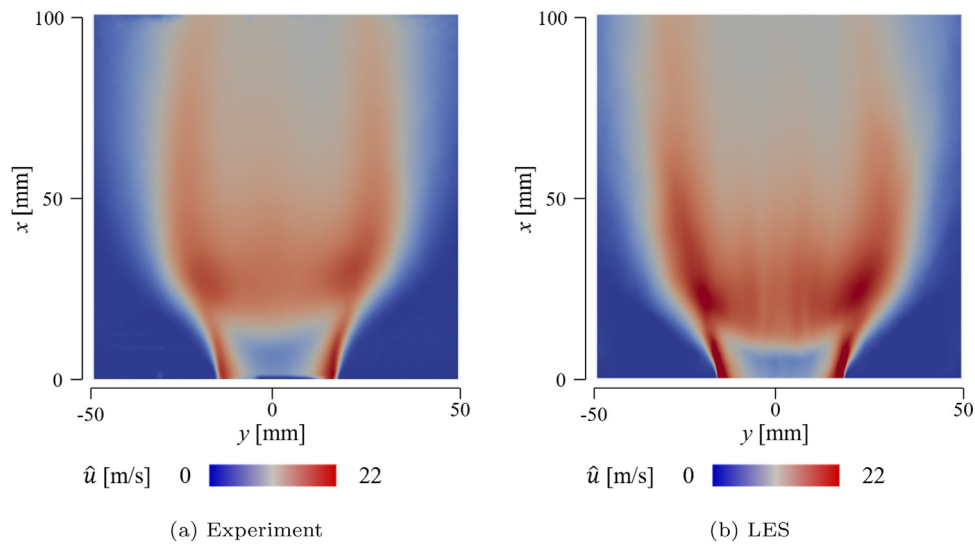

(a) Experiment   (b) LES

Fig. 7. Comparison of time-averaged axial velocity distributions in the central $x - y$ plane ($z = 0$ mm) between experimental data and LES prediction.
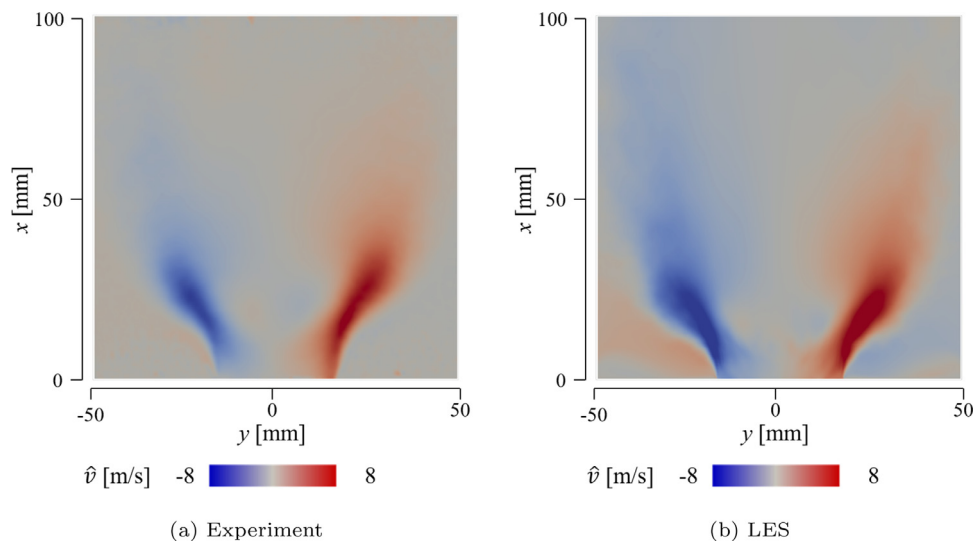

(a) Experiment   (b) LES

Fig. 8. Comparison of time-averaged radial velocity distributions in the central $x - y$ plane ($z = 0$ mm) between experimental data and LES prediction.
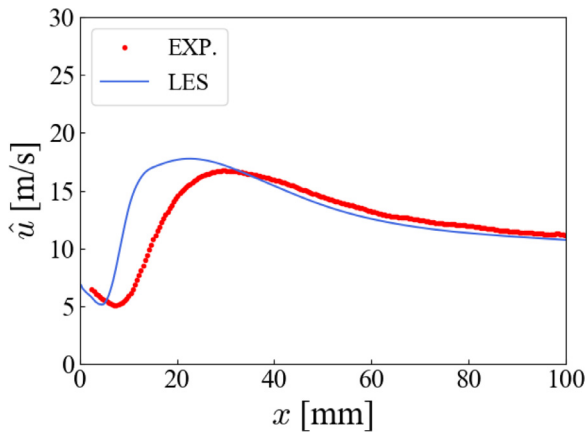
Fig. 9. Comparison of axial profiles of time-averaged axial velocity along the burner axis (i.e, $y = z = 0$ mm) between experimental data and LES prediction.

dependence into account are computed according to CHEMKIN [50,51].

For simulating acoustic wave propagation all the way up to the far-field, the CAA solver of the FK^3-CAA code employs the 4th order accurate Dispersion-Relation-Preserving (DRP) scheme of Tam and Webb [52] for discretization of the spatial derivatives on the left-hand side of the APE-RF, and the two-step alternating low-dissipation and low-dispersion Runge-Kutta (LDDRK) scheme in the 5–6 configuration [53] for temporal discretization. The low-pass filtering method of Artificial Selective Damping (ASD) proposed by Tam and Shen [54] for suppressing spurious high-frequency waves is also used in the CAA solver. The complete CPU time required for the hybrid LES/APE-RF simulation (i.e., the time needed for the ini-

tial LES for computing $\hat{\rho}$, $\hat{\boldsymbol{u}}$ and $\hat{c}$, plus the time for the combined LES/APE-RF computations) is approximately 1.2 Million hours, by parallel computation using 1000 cores on a CRAY XC40 supercomputer at the Academic Centre for Computing and Media Studies (ACCMS), Kyoto University, Japan.

In this study, three CAA cases are simulated, each with different acoustic source terms to investigate their influence on the acoustic field. Table 1 summarizes the acoustic source terms considered in each CAA simulation case. In case1, the APE-RF system is solved by considering all three acoustic source terms $q_{e,rf}$, $\boldsymbol{q}_{m,rf}$ and $q_{c,rf}$. In case2, the acoustic source term $q_{e,rf}$ of the pressure-density relation in Eq. (9) alone is considered, and in case3, only the acoustic source term $\boldsymbol{q}_{m,rf}$ on the RHS of the perturbation velocity $\boldsymbol{u}'$ equation, i.e. Eq. (8), is considered.

3. Results and discussion

3.1. Combustion field results

First, the combustion field of the open LPHALS turbulent flame predicted by the LES is investigated. Instantaneous distribution of the iso-surface of temperature at 1500 K (colored in blue) is depicted in Fig. 5(a), while the instantaneous distributions of the iso-surfaces of heat release rate and the second invariant of the velocity gradient tensor Q_2 are illustrated in Fig. 5(b). The iso-surfaces of Q_2 represent the turbulent flow structures, and in Fig. 5(b), the iso-surfaces of Q_2 are depicted for a positive value, i.e., for $Q_2 > 0$, which indicate the vorticity-dominated regions. Additionally, the instantaneous temperature field in the central $x - y$ plane (i.e., $z = 0$ mm) is shown in Fig. 6(a). From these figures, it is evident that a lifted flame is formed above the burner exit. Interactions of the turbulent structures formed in the shear layers with the flame front, which can be observed in Fig. 5(b), produce deformations
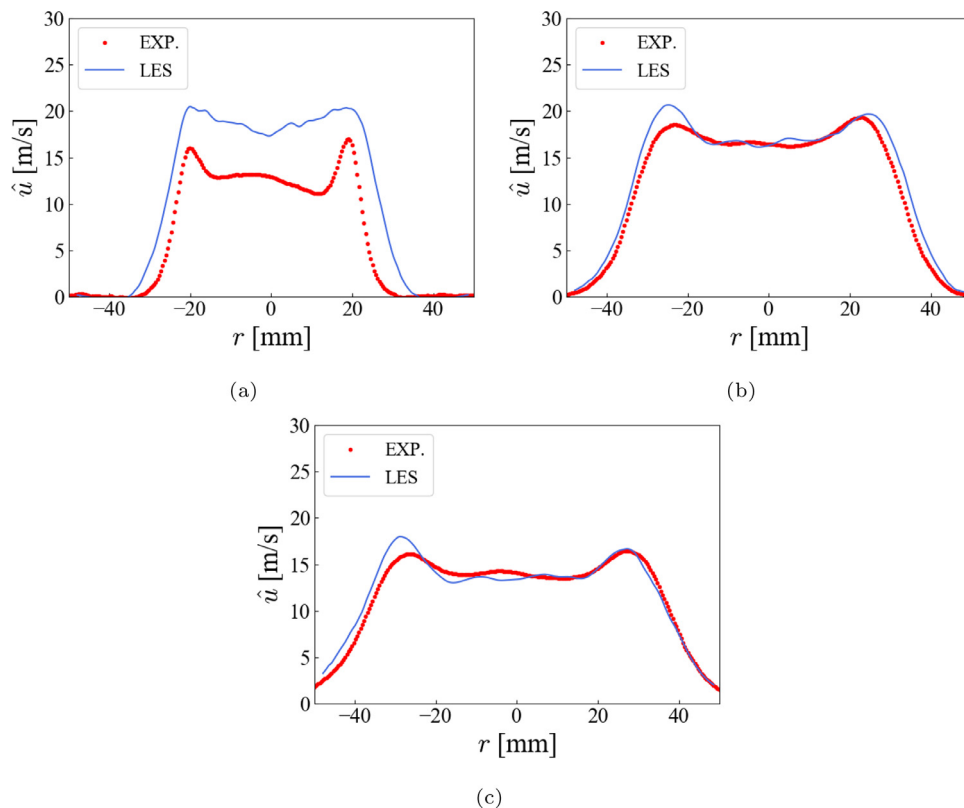

(a)

(b)

(c)

Fig. 10. Comparisons of radial profiles of time-averaged axial velocity between experimental data and LES predictions at different stream-wise locations of (a) $x = 17.5$ mm, (b) $x = 35$ mm and (c) $x = 52.5$ mm.

Fig. 11. Comparisons of radial profiles of time-averaged radial velocity between experimental data and LES predictions at different stream-wise locations of (a) $x = 17.5$ mm, (b) $x = 35$ mm and (c) $x = 52.5$ mm.
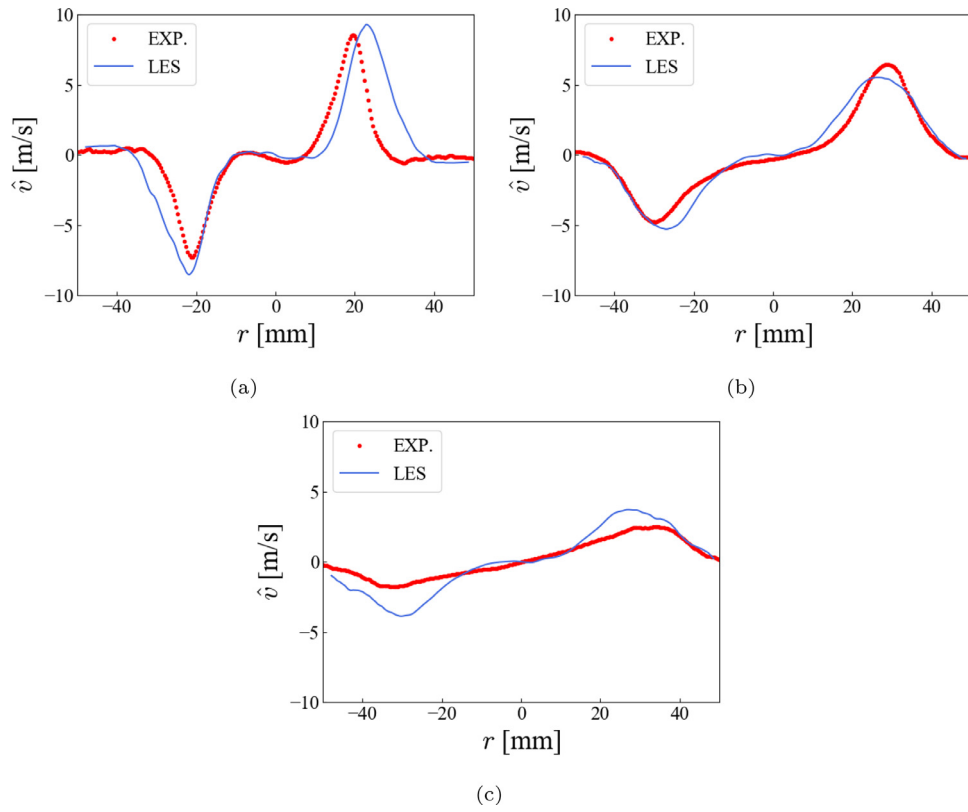

Fig. 12. Comparisons of radial profiles of RMS of axial velocity fluctuations between experimental data and LES predictions at different stream-wise locations of (a) $x = 17.5$ mm, (b) $x = 35$ mm and (c) $x = 52.5$ mm.

Fig. 13. Comparisons of radial profiles of RMS of radial velocity fluctuations between experimental data and LES predictions at different stream-wise locations of (a) $x = 17.5$ mm, (b) $x = 35$ mm and (c) $x = 52.5$ mm.

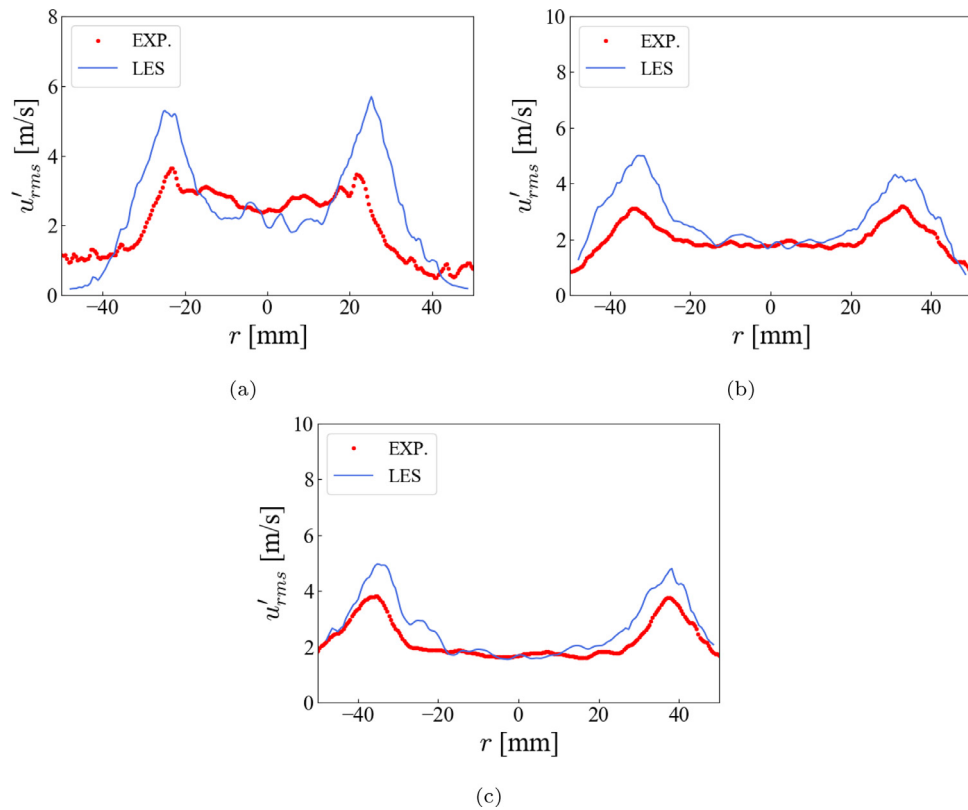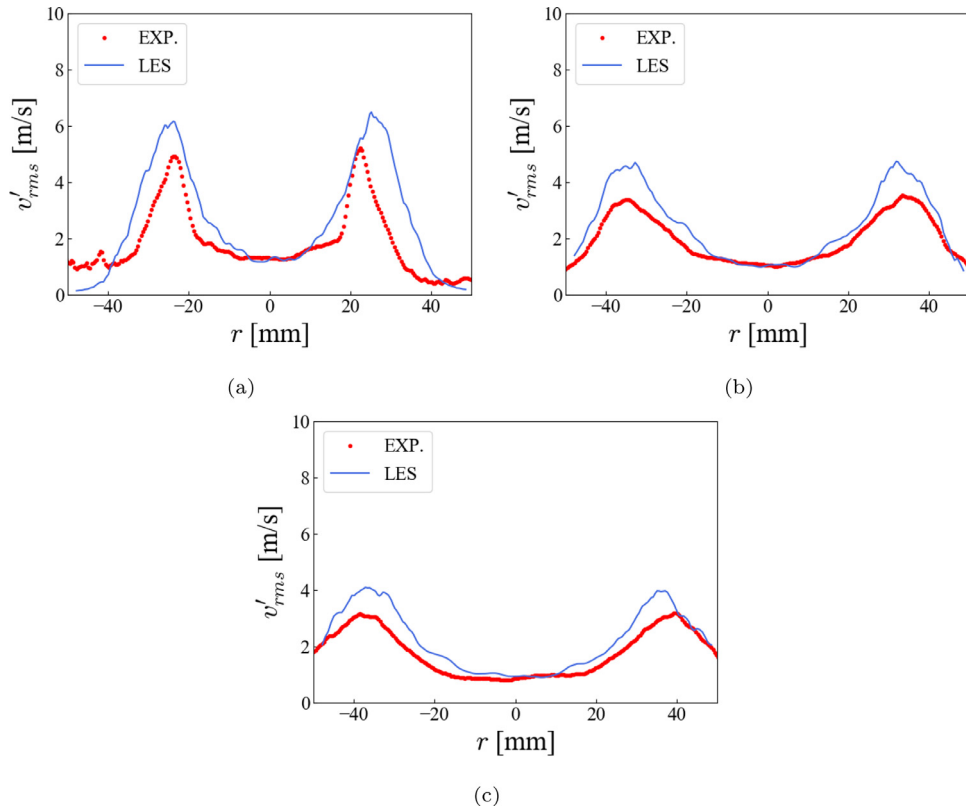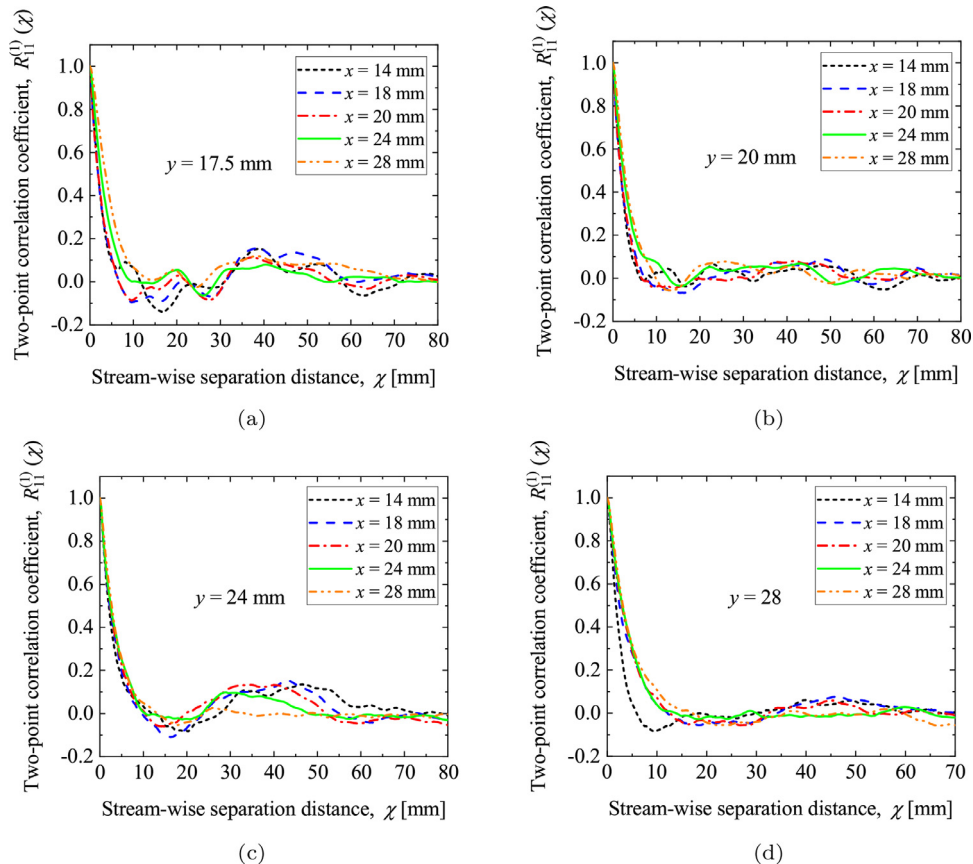**Fig. 14.** Stream-wise profiles of the two-point correlation coefficient of axial velocity fluctuations $R_{11}^{(1)}(\chi)$ computed for various stream-wise locations ($x = 14$ mm, 18 mm, 20 mm, 24 mm and 28 mm) at the radial locations of (a) $y = 17.5$ mm, (b) $y = 20$ mm, (c) $y = 24$ mm and (d) $y = 28$ mm.

京都大学
KYOTO UNIVERSITY

A.L. Pillai, S. Inoue, T. Shoji et al.

Combustion and Flame 245 (2022) 112360

京都大学学術情報リポジトリ
KURENAI 紅
Kyoto University Research Information Repository

of the flame surface. Such flame deformations caused by the flow-field turbulence can also be clearly discerned from the temperature iso-surface shown in Fig. 5(a). The flame considered in this study is a low-swirl flame with a swirl number of 0.39. In this flame, vortex breakdown does not occur owing to its relatively weak swirling motion. Vortex breakdown occurs when the swirl number/intensity exceeds a specific threshold, typically for swirl numbers greater than 0.5 [55]. Therefore, in the absence of vortex breakdown, flow structures such as the central recirculation zone and the precessing vortex core are not formed in the LPHALS flame investigated in this study, nor were they formed in the experiment [21]. On the contrary, in such low-swirl flames, the axial flow velocity decays along the stream-wise direction with increasing downstream distance from the burner exit (as will be shown later) within the central divergence zone (CDZ) [21]. Thus, the lifted flame can freely propagate upstream (against the divergent flow) towards the burner exit, and can stabilize aerodynamically at the location where the local flow velocity equals the burning velocity. Figure 6(b) depicts the time-averaged temperature field in the central $x - y$ plane obtained from the LES, and the maximum mean flame temperature predicted by the LES is 1534 K, which agrees well with the flame temperature of 1530 K obtained from the 1D laminar premixed flame computation described in Section 2.1.1.

Next, the LES results for velocity field are examined. Comparisons of the distributions of time-averaged axial and radial velocity components in the central $x - y$ plane between measurements and LES predictions are illustrated in Figs. 7 and 8, respectively. These figures show that the distributions of mean axial and radial velocity components obtained from the LES are in good qualitative agreement with experimental data. The LES predicted time-averaged axial velocity distribution in Fig. 7(b) shows the formation of a central divergence zone (a characteristic flow structure of low-swirl flames) similar to that observed in the experimental data, i.e., in Fig. 7(a). Owing to the heat release accompanying combustion and the consequent thermal expansion, there is an increase in the axial velocity across the flame front, followed by the decay of axial velocity along the axial direction, downstream of the flame front. Additionally, upon comparing the LES predicted time-averaged radial velocity distribution in Fig. 8(b) with the corresponding experimental data in Fig. 8(a), it can be confirmed that the radial spread of the LPHALS flame is well reproduced by the LES.

Quantitative comparison of the velocity field obtained from the LES with that measured in the experiment are presented in the following. Figure 9 shows the comparison of axial profile of time-averaged axial velocity along the burner axis computed in the LES, with that measured in the experiment. The peak value of mean axial velocity predicted by the LES agrees reasonably well with that
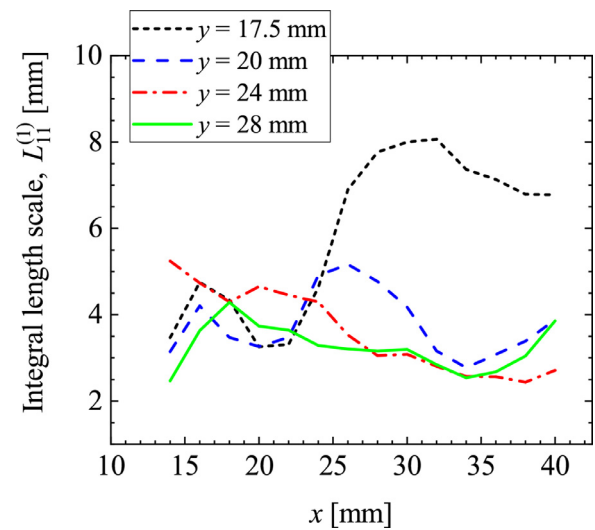

Fig. 15. Evolution of the integral length scale $L_{11}^{(1)}$ along the stream-wise direction, computed at the same radial locations as those considered in Fig. 14.

in the experiment, and the axial profile of mean axial velocity is accurately reproduced by the LES for $x \geq 30$ mm. However, the axial location of the LES predicted peak mean axial velocity is shifted slightly upstream of that in the experiment. This discrepancy is attributed to the fact that the turbulent inflow velocity boundary conditions applied at the burner exit in the LES, do not completely match with those in the experiment, because the complex LSB geometry situated upstream of the burner exit is excluded from the LES. Next, in Figs. 10 and 11, the radial profiles of time-averaged axial velocity and radial velocity components obtained from the LES are compared with the corresponding experimental measurements at different stream-wise locations from the burner exit. In Fig. 10(a), it can be seen that the axial velocity is overestimated at the stream-wise location of $x = 17.5$ mm, but the LES predicted radial profiles of axial velocity at the other stream-wise locations conform well with the measurements, while also capturing the radial locations of the peak axial velocities in these radial profiles and the flame spread accurately. Similar tendencies are observed in the LES predicted radial profiles of radial velocity in Fig. 11. Hence, from the results presented in Figs. 10 and 11, it can be said that the LES predictions are in an overall favourable agreement with the experimental data. Additionally, the radial profiles of root mean square (RMS) fluctuation of axial velocity and radial velocity computed from the LES are compared with the corresponding experimental data in Figs. 12 and 13, respectively. The stream-wise lo-
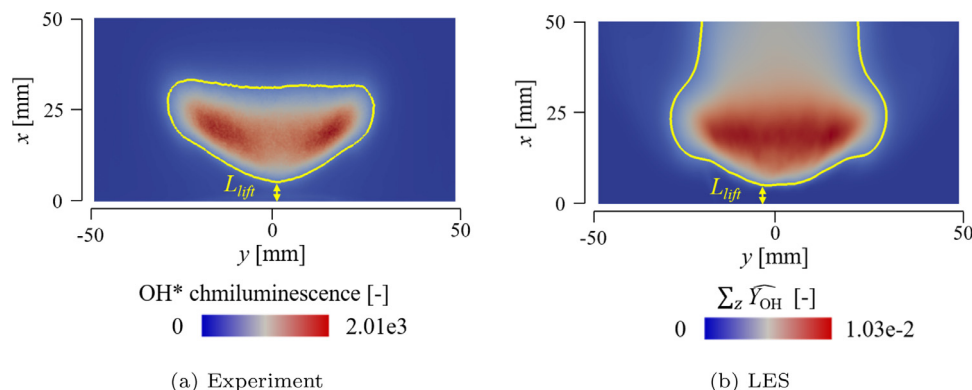

(a) Experiment

(b) LES

Fig. 16. Time-averaged distributions of experimental OH* chemiluminescence [21] (left), and computed line of sight integrated mean OH radical mass fraction, $\sum_z \widehat{Y_{OH}}$ (right) on the $x - y$ plane. Yellow lines indicate the isolines of 20% of the maximum mean value of OH* chemiluminescence (left) and $\sum_z \widehat{Y_{OH}}$ (right).

cations at which these comparisons are performed, are the same as those in Figs. 10 and 11. Though there are some discrepancies in the radial profiles of RMS fluctuations of axial and radial velocities predicted by the LES (especially in the shear layers), their tendencies such as the LPHALS flame's radial spread and the radial locations of the peak RMS fluctuations of velocity components, are in favourable agreement with the tendencies observed in the measurements. As mentioned above, an important reason for the over-predictions of u'_{rms} and v'_{rms} in the shear layers by the LES, is the lack of the complex LSB geometry situated upstream of the burner exit, in the LES's computational domain. However, there is another reason for these discrepancies between the LES and experimental results. In the experiment, vector calculation from particle images acquired by Particle Image Velocimetry (PIV) measurements is essentially a spatial correlation analysis involving spatial interrogation. In the flow-field where there is a large velocity gradient within a relatively small spatial domain, e.g., shear layers in the present study, an interrogation domain cannot very finely capture the velocity gradient, and hence the resultant peak velocity fluctuation amplitudes and the widths of the peaks typically become smaller and larger, respectively, than the true values. In the present study, the RMS fluctuations of the velocity components have some discrepancies between the experimental and numerical results in the shear layers, where the situation described above occurs. Therefore, these discrepancies may also be caused by the interrogation analysis used in the vector calculation in the experiment.

In order to obtain more insights into the turbulent state of the LPHALS flame, the spatial variations of two-point correlation coefficient of the axial velocity fluctuations and the evolution of the integral length scale in the shear layers are examined next. Figure 14 presents the stream-wise variations of the two-point correlation coefficient of the axial velocity fluctuations $R^{(1)}_{11}(\chi)$, computed at various stream-wise locations (x) for a given radial location (y). Here, $R^{(1)}_{11}(\chi)$ is defined as follows:

$$R^{(1)}_{11}(\chi) = \frac{\langle u'(x,y,z) \times u'(x+\chi,y,z)\rangle}{u'_{rms}(x,y,z) \times u'_{rms}(x+\chi,y,z)} \quad (14)$$

where u' is the axial velocity fluctuation given as $u' = \tilde{u} - \hat{u}$, χ is the separation distance in the stream-wise x-direction, and the angle brackets $\langle\rangle$ in the numerator of Eq. (14) represent temporal averaging. The radial locations chosen for this analysis are such that the interrogation positions (x, y) in Fig. 14 lie in the shear layers of the LPHALS flame, where the turbulent structures interact with the flame front. Hence, the $R^{(1)}_{11}(\chi)$ distributions presented in Fig. 14 also offer a signature of the spatial extend of the acoustic source terms in the stream-wise direction, at the respective interrogation positions. The stream-wise variations of $R^{(1)}_{11}(\chi)$ differ with the radial location (y) in the shear layers at which they are evaluated, owing to the influence of heat release and entrainment of the surrounding ambient air into the swirling flame. A key observation from these stream-wise variations of $R^{(1)}_{11}(\chi)$ is that, negative values of $R^{(1)}_{11}(\chi)$ can be found at several interrogation positions, which is probably an indication of periodicity in the shear layers. In the analysis presented later in Section 3.3, there is indeed evidence of periodic interactions between the turbulent flow structures and the flame front in the shear layers. Spatial evolution of the integral length scale $L^{(1)}_{11}$ along the stream-wise x-direction, at the same radial locations where $R^{(1)}_{11}(\chi)$ is computed in Fig. 14, are depicted in Fig. 15. Here, the integral length scales $L^{(1)}_{11}$ are computed from the stream-wise distributions of $R^{(1)}_{11}(\chi)$ as $L^{(1)}_{11} = \int_0^\infty R^{(1)}_{11}(\chi)d\chi$. It is evident from Fig. 15 that the stream-wise evolution of $L^{(1)}_{11}$ differs with the radial location at which it is evaluated. As will be shown later in Section 3.3, an important heat release rate fluctuation phenomenon occurring in the shear layer
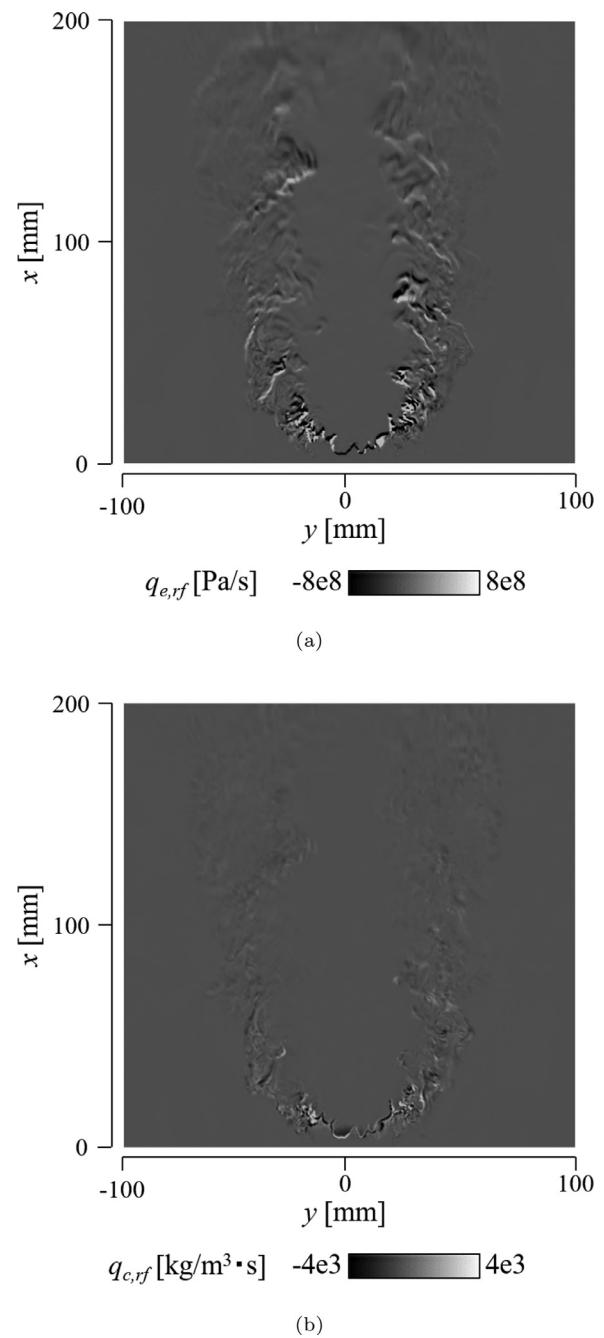

$q_{e,rf}$ [Pa/s]   -8e8 ▮▮▮▮ 8e8

(a)

$q_{c,rf}$ [kg/m³·s]   -4e3 ▮▮▮▮ 4e3

(b)

Fig. 17. Instantaneous distributions of acoustic source terms (a) $q_{e,rf}$ and (b) $q_{c,rf}$ in the $x - y$ plane ($z = 0$ mm), obtained from LES solution.

region for stream-wise locations within 16 mm $\leq x \leq$ 26 mm, is partly responsible for a pronounced peak at a specific frequency in the spectra of combustion noise generated by this open LPHALS flame. Similar to the interrogation positions for $R^{(1)}_{11}(\chi)$ computations, the positions considered in Fig. 15 for estimating $L^{(1)}_{11}$, especially for the stream-wise locations within 14 mm $\leq x \leq$ 26 mm, lie in the shear layer region where flame-turbulence interactions occur. Thus, the results in Fig. 15 provide an estimate of the sizes of the integral length scales $L^{(1)}_{11}$ interacting with the flame front and causing heat release rate fluctuations along the flame front. Furthermore, for the positions at which $L^{(1)}_{11}$ is computed in Fig. 15, the LES grid is discretized by a uniform grid spacing of 300 μm, so these integral length scales are adequately resolved.
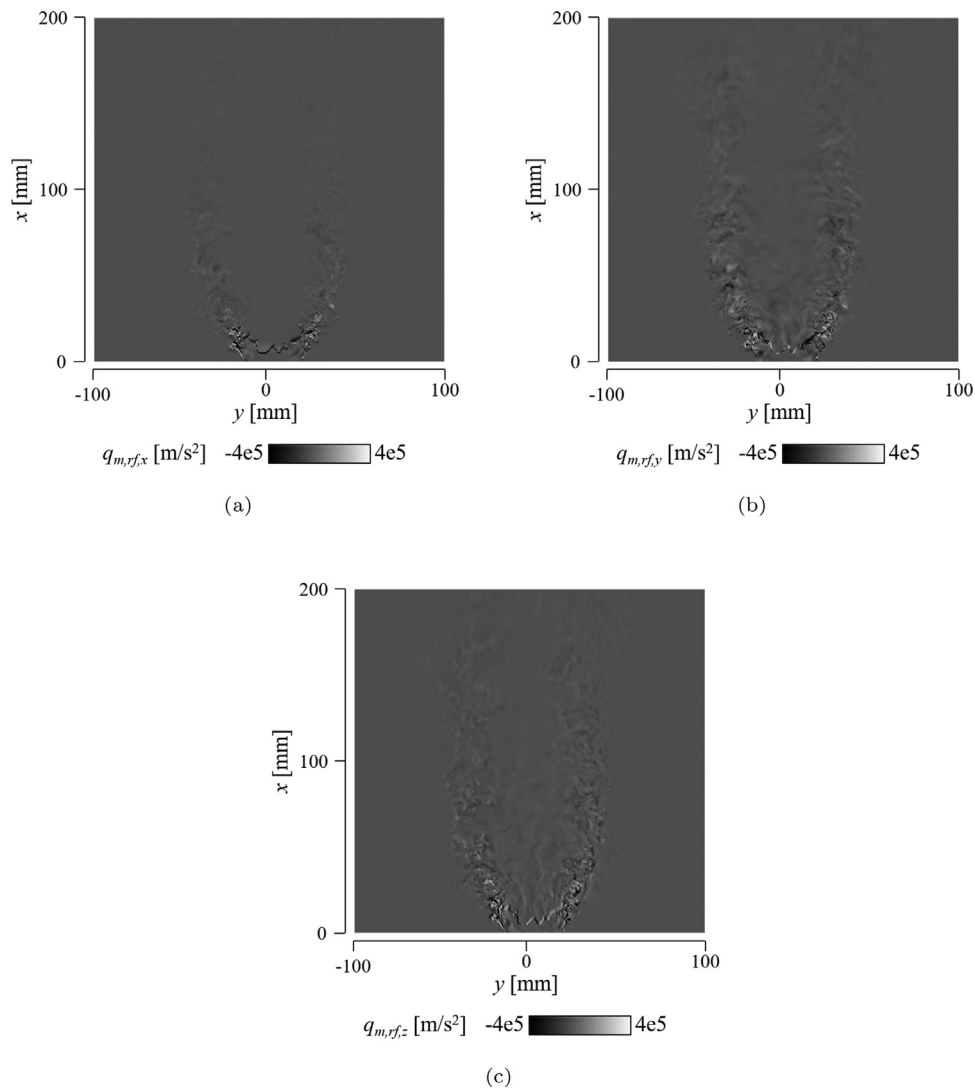
Fig. 18. Instantaneous distributions of the components of acoustic source term $\boldsymbol{q}_{m,rf}$ in the $x-y$ plane ($z = 0$ mm), obtained from LES solution.

To investigate the prediction accuracy of the flame's lift-off height L_{lift}, Fig. 16 depicts the comparison of the line of sight integrated mean (i.e., time-averaged) OH* chemiluminescence distribution measured in the experiment, with the line of sight integrated mean (i.e., time-averaged) OH radical mass fraction distribution, i.e., $\sum_z \widehat{Y_{OH}}$, on the $x-y$ plane obtained from the LES. The detailed reaction mechanism [33] adopted for generating the flamelet library for the LES does not contain the OH* species, so the mass fraction of OH radical is used for the comparison instead. Consequently, the distribution of mean OH radical mass fraction shown in Fig. 16(b) will differ from that of the mean OH* chemiluminescence measured in the experiment. However, the LES correctly predicts the V-flame structure observed in the experiment. In this study, the flame lift-off height L_{lift} is defined as the minimum height from the burner exit to the isoline of 20% of the maximum mean OH radical mass fraction, which is denoted by the yellow isoline in Fig. 16(b). In the experiment, 20% of the maximum mean OH* chemiluminescence intensity, which is denoted by the yellow isoline in Fig. 16(a), was used as the threshold value for defining L_{lift} [21]. Flame lift-off height evaluated from the LES using the metric defined above is $L_{lift} = 5.25$ mm, while that measured in the experiment is $L_{lift} = 5.39$ mm [21]. Thus, the flame lift-off height predicted by the LES is in good agreement with that of the actual open LPHALS flame. Based on the LES results for the

first and second order velocity statistics shown in Figs. 10–13, and the flame structure and lift-off height predictions in Fig. 16, it can be said that the LES in this study is capable of reproducing the combustion field of the open LPHALS flame with reasonable accuracy. Temperature profiles were not measured in the experiment, and hence we were unable to compare the LES predicted temperature profiles with those of the real flame.

In Section 2.3, it was mentioned that the adiabatic boundary condition is imposed on the annular metal base-plate around the burner exit (i.e., the annular grey patch surrounding the burner exit in Fig. 3). It should be noted that the current study deals with an open lifted lean-premixed low-swirl flame, wherein the flame does not interact directly with this annular metal base-plate, nor is the flame attached to the burner exit periphery. Additionally, there is a continuous supply of cold premixed gas at 300 K flowing out from the burner exit towards the flame. Consequently, convection and conduction heat transfer from the flame to the annular metal base-plate is unlikely. The main mode of heat transfer from the flame to the base-plate will therefore be radiative heat transfer. But it should also be noted that a lean-premixed H_2/air flame is considered in this study, which is a non-sooty flame, so it mainly emits radiation in the infrared spectrum. However, every time the LSB was operated in the experiment to measure certain quantities, the data sampling would be completed fairly quickly, usually in

about 10–20 s. Therefore, within this short time duration, infrared radiation from the flame to the annular metal base-plate is unlikely to cause any drastic temperature variations on the base-plate's surface. Consequently, the likelihood of the base-plate's surface temperature influencing the temperature field of the gas in its vicinity, which will have a subsequent impact on the flame lift-off height or the flame's distance from the annular metal base-plate, is also expected to be insignificant. Hence, conjugate heat transfer between the flame and the annular metal base-plate (via. radiative heat transfer from the flame) is not considered in the current LES. Furthermore, temperature distribution on the metal base-plate's surface was not measured in the experiment, and hence the adiabatic boundary condition is imposed on the annular metal base-plate's surface in the LES. Moreover, from the temperature distributions illustrated in Fig. 6, it can be substantiated that even with the adiabatic wall surface assumption, the temperature close to the burner exit periphery and the annular metal base-plate remains more or less the same as the ambient temperature of 300 K.

3.2. Acoustic field generated by the open LPHALS flame

Results of the CAA simulation case that considers all the acoustic source terms of the APE-RF system (i.e., $q_{c,rf}$, $\boldsymbol{q}_{m,rf}$ and $q_{e,rf}$), viz. case1 (see Table 1), are examined and an analysis of these acoustic source terms is also presented in the following. Figures 17 and 18 illustrate the instantaneous distributions of the three types of acoustic source terms in the system of APE-RF, viz. $q_{e,rf}$, $q_{c,rf}$ and $\boldsymbol{q}_{m,rf}$, respectively, in the central $x - y$ plane. These source terms are computed from the LES solution and interpolated onto the CAA grid from the LES grid at the end of every LES step, to solve the APE-RF system in the CAA step. From Figs. 17 and 18, it is evident that $q_{c,rf}$ is 5 orders of magnitude smaller than $q_{e,rf}$, and all three components of the source term $\boldsymbol{q}_{m,rf}$ are 3 orders of magnitude smaller than $q_{e,rf}$. Hence, the acoustic source term $q_{e,rf}$ which is the strongest, is expected to have a dominant contribution to the acoustic field, while the influence of the other two sources terms, i.e., $\boldsymbol{q}_{m,rf}$ and $q_{c,rf}$, on the acoustic field is expected to be insignificant in comparison. An analysis on this is presented in the next subsection. Instantaneous distributions of the dominant acoustic source term $q_{e,rf}$ and the heat release rate per unit volume Q in the central $x - y$ plane are shown in Fig. 19. Comparing Figs. 17(a) and 19, it can be discerned that the regions where $q_{e,rf}$ is particularly strong, coincide with those where the unsteady heat release of combustion occurs. This observation is consistent with the formulation of the acoustic source term $q_{e,rf}$, because as mentioned previously in Section 2.2, the substantial time derivative of density ($D\rho/Dt$) term on the RHS of Eq. (12) includes the dominant source mechanism of direct combustion noise, i.e., the unsteady heat release [25,38]. Furthermore, Fig. 20 depicts the instantaneous acoustic pressure perturbation p' fields obtained from the CAA simulation (represented in grey scale), along with the instantaneous distributions of the dominant acoustic source term $q_{e,rf}$, in the central $x - y$ plane and the $y - z$ plane at $x = 20$ mm of the CAA grid. Excitation of strong pressure perturbations in the regions where $q_{e,rf}$ is large, is evident from the pressure perturbation field in the central $x - y$ plane (Fig. 20). Additionally, it is observed that the acoustic pressure perturbations propagate almost circularly in the $y - z$ plane, owing to the circular distribution of $q_{e,rf}$ in the $y - z$ plane, which arises due to the axisymmetric feature of the low-swirl flame.

CAA simulation case1's results for the radiated acoustic field are compared with those of Shoji et al.'s experiment [21] next. Sound pressure level (SPL) spectra computed from the solution of the APE-RF in CAA simulation case1, are compared with the measured SPL spectra in Fig. 21 for two positions: $(x, y) = (50$ mm, 180 mm$)$ and $(x, y) = (50$ mm, 360 mm$)$. These two positions are also indi-
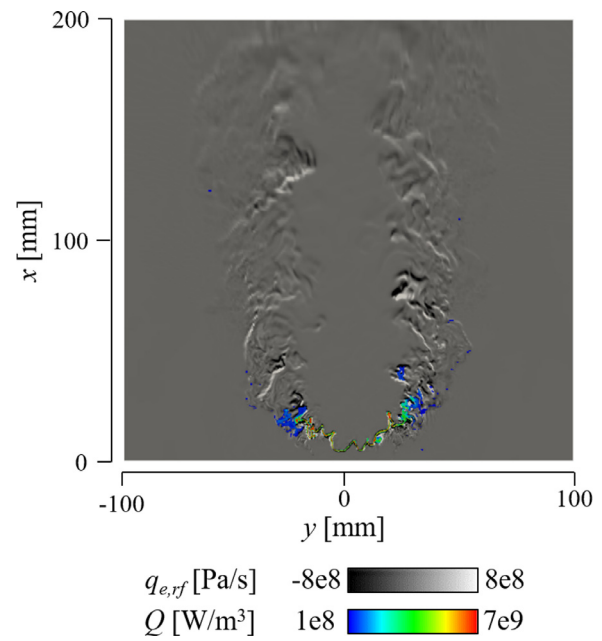

Fig. 19. Instantaneous distributions of acoustic souce term, $q_{e,rf}$ and heat release rate, Q in the $x - y$ plane ($z = 0$ mm).
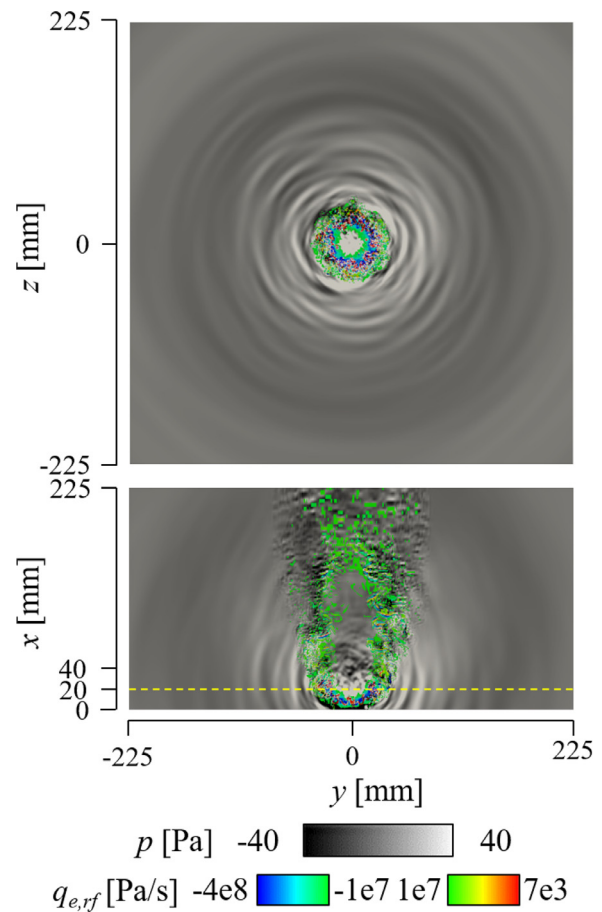

Fig. 20. Instantaneous distributions of acoustic pressure perturbation, p' (obtained from CAA solution), and acoustic source term, $q_{e,rf}$ (obtained from the LES solution) in the $x - y$ plane at $z = 0$ mm (below), and the $y - z$ plane (represented by the yellow dashed line in the $x - y$ plane) at $x = 20$ mm (above), of the CAA grid. (For interpretation of the references to colour in this figure legend, the reader is referred to the web version of this article.)
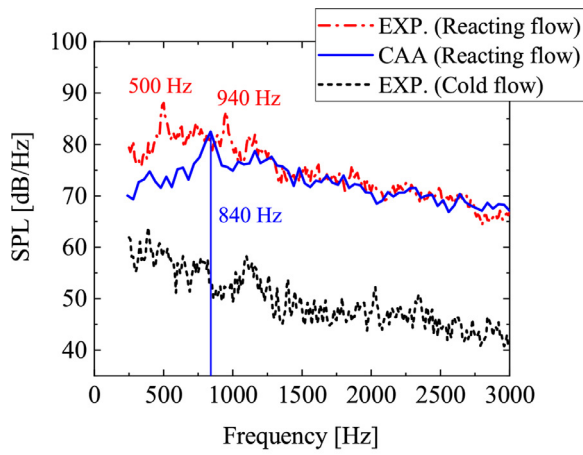
(a) $(x, y) = (50\ \text{mm}, 180\ \text{mm})$
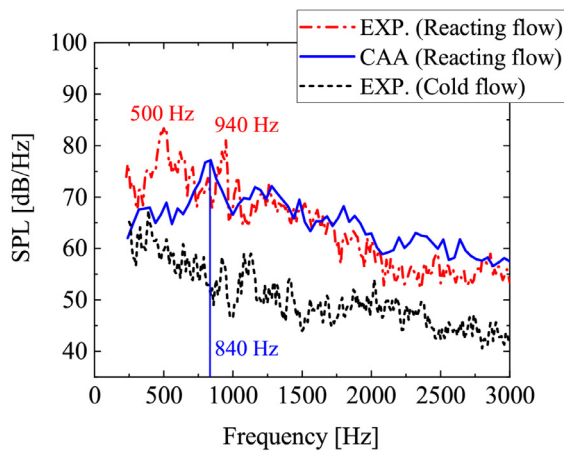
(b) $(x, y) = (50\ \text{mm}, 360\ \text{mm})$

Fig. 21. Comparisons of sound pressure level (SPL) spectra between experimental data [21] and CAA predictions at different positions.

Fig. 22. Sketch of positions (red and green circular points) in the $x - y$ plane ($z = 0$ mm) at which SPL spectra are computed. Distribution of the time-averaged speed of sound $\hat{c}$ (obtained from the LES) in this $x - y$ plane is also shown. (For interpretation of the references to colour in this figure legend, the reader is referred to the web version of this article.)

Fig. 23. Stream-wise variation of the spectrum of coherence $C_{q'_{rad} p'}(x, f)$ between the radially integrated heat release rate fluctuations $q'_{rad}(x)$ and the far-field acoustic pressure perturbations p' sampled at $(x, y) = (50\ \text{mm}, 180\ \text{mm})$.

cated by the two green circular points in Fig. 22, and are the same positions at which microphones were placed in the experiment. Noise spectra of the non-reacting low-swirl flow that were measured before igniting the H_2/air premixed gas in the experiment, are also plotted for comparison. It can be seen from Fig. 21 that for the frequencies below 1800 Hz (i.e., for most frequencies of interest), the Sound Pressure Levels (SPLs) of the non-reacting flow are about 20–25 dB lower than those of combustion noise (i.e., the reacting flow) in the experiment. This observation is consistent with the findings reported in several previous studies (e.g., [9,13,27,56–59]), that in low Mach number open turbulent flames, the noise generated by the unsteady heat release dominates over turbulent mixing noise. In Fig. 21, it is observed that the computed SPL spectra show favourable agreement with the measured SPL spectra for frequencies greater than 1000 Hz (i.e., $f > 1000$ Hz). However, for frequencies below 1000 Hz, the computed SPLs are under-predicted and the first pronounced peak at $f = 500$ Hz, which is observed in the measured combustion noise spectra is not captured. The two pronounced SPL peaks at 500 Hz and 940 Hz measured in the experiment, are generally not observed in the spectra of direct combustion noise radiated by open flames. Such pronounced twin spectral peaks are unique to the low-swirl lean-premixed H_2/air flames investigated by Shoji et al. [21], and based on their investigation, the SPL peak at 500 Hz was caused by global
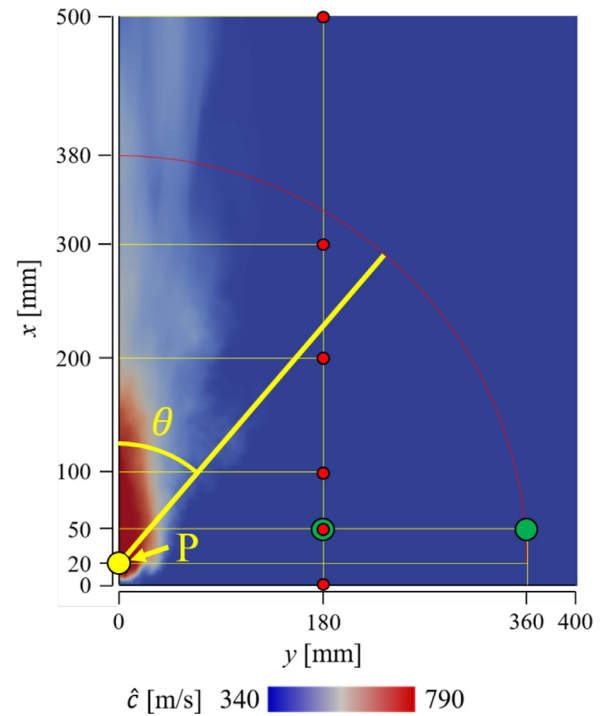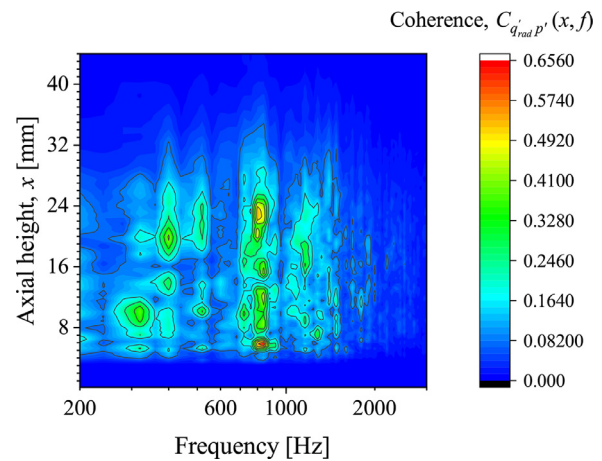
flame fluctuations that induced global heat release fluctuations at the same frequency. At this stage, it is important to clarify the following aspects:

1. It is known from previous numerical studies (e.g., [24,27,60]) that the exclusion of even a part of the burner geometry from the computational configuration can affect the prediction accuracy of the hybrid LES/APE-RF simulation, because the acoustic modes of the burner can interact with the turbulent flame and influence its dynamics and combustion noise.

2. However, in Shoji et al.'s experiments [21], the LSB system, or the entire experimental system for that matter, does not have natural frequencies in the range of the double peak frequencies (i.e., 500 Hz and 940 Hz). Therefore, the acoustic pressure
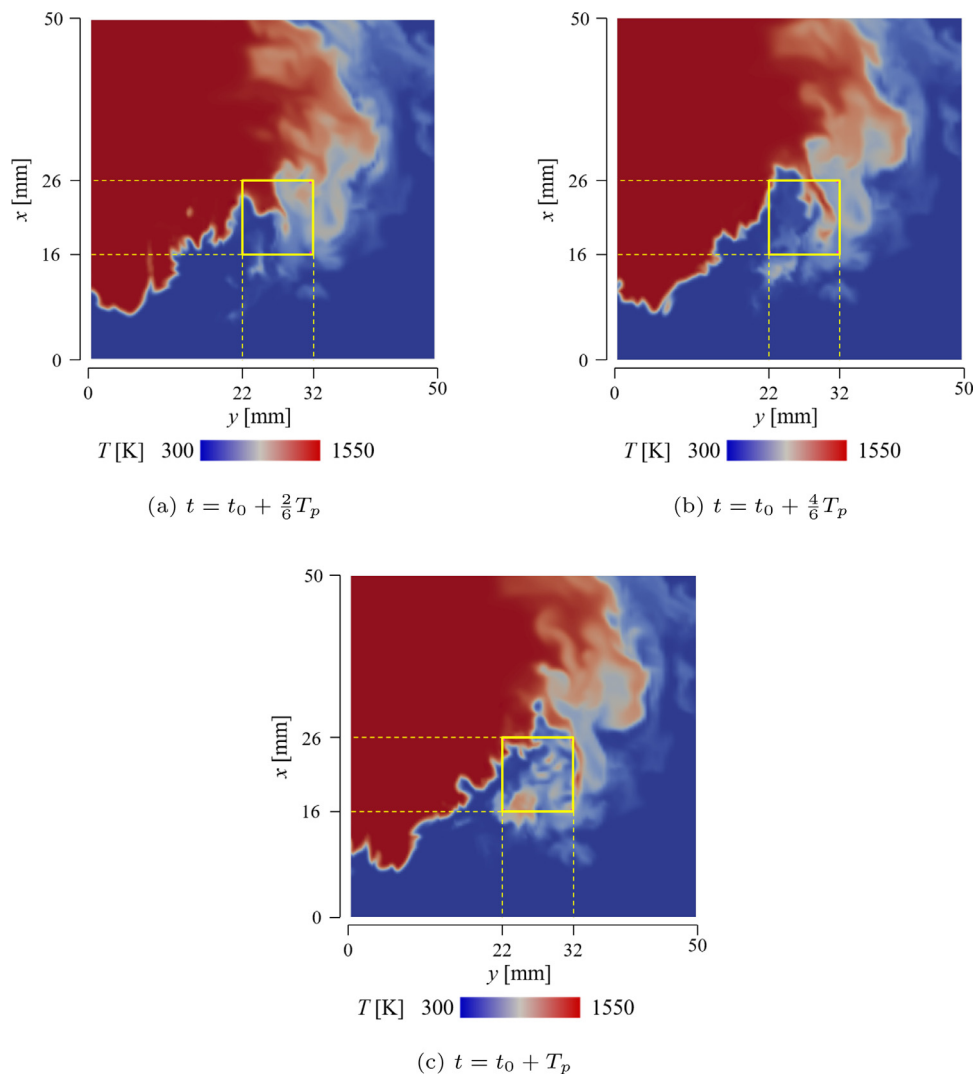
(a) $t = t_0 + \frac{2}{6} T_p$

(b) $t = t_0 + \frac{4}{6} T_p$

(c) $t = t_0 + T_p$

Fig. 24. Flame structures observed in the instantaneous temperature distributions on the $x - y$ plane ($z = 0$ mm), extracted over a time period of $T_p = 1/840$ s, with the interrogation window (yellow square) situated at $(x, y) = (22–32$ mm, $16–26$ mm). t_0 is an arbitrary time at which LES data sampling starts. (For interpretation of the references to colour in this figure legend, the reader is referred to the web version of this article.)

waves generated by the flame do not couple with the LSB system's acoustics, and do not cause any pulsations in the flow rate of the premixed gas mixture supply upstream of the burner exit, at a frequency corresponding to that of the double peaks observed in the experiment.

3. If relatively high-frequency fluctuations of the premixed gas mixture were strong in the LSB system, they would be removed by the two flow screens or punching plates placed inside the burner, as shown in Fig. 2.

4. Additionally, the air compressor used in the experiment, which can cause flow fluctuations, was placed very far from the burner system. In between them, there is long piping, which would eliminate flow fluctuations that were strongly oscillating at a single frequency, if they existed.

5. Furthermore, an air reservoir with a large volume was placed downstream of the air compressor as a buffer, to remove any periodic fluctuations associated with the compressor frequency.

6. Overall, no fluctuations occurring upstream of the burner exit caused pronounced, sharp double peaks in the combustion noise spectra. Rather, these twin spectral peaks in the measured combustion noise spectra were caused purely by physical phenomena in the flow field present downstream of the burner exit [21].

The present CAA simulation is unable to predict the SPL peak at 500 Hz and underestimates the SPLs for $f < 1000$ Hz. These discrepancies are attributed to the inflow boundary conditions for the turbulent velocity field applied at the burner exit in the LES, which do not completely match with those in the experiment. This is because the present LES domain lacks the full LSB geometry situated upstream of the burner exit to keep the computational cost realizable (see Section 2.3). Thus, the heat release rate fluctuations, which are extremely sensitive to the inflow turbulent velocity fluctuations and are the dominant source mechanism of direct combustion noise, will not be perfectly predicted by the present LES.

Furthermore, it is worth noting that, while the combustion noise spectra measured in the experiment are estimated using the pressure perturbation p' signals sampled over a time duration of 5 s, those obtained from the CAA simulation are computed using p' signals sampled over 0.3 s duration. Therefore, owing to the nature of combustion noise, characteristics of the combustion noise spectra (such as amplitude and peak presence) can slightly vary, both qualitatively and quantitatively, depending on the time period of the p' signal within which the spectra are estimated. For instance, even when using the same experimentally obtained p' signal, the amplitude of the SPL peak at 500 Hz and its presence can vary if the entire 5 s signal is used, as in Shoji et al.'s study [21], or

only a portion of the signal is used, e.g., 0.3 s duration, as done in the present CAA simulation. Hence, this is another likely reason as to why the CAA simulation is unable to predict the SPL peak at 500 Hz observed in the experimental combustion noise spectra. However, as depicted in Fig. 21, the CAA simulation can predict the reduction in SPLs with increasing radial distance (y) from the burner axis (i.e., $y = 0$ mm), and the amount by which the SPLs reduce when the observer position changes from $(x, y) = (50$ mm, 180 mm) to $(x, y) = (50$ mm, 360 mm), agrees well with that in the experiment. Moreover, the CAA simulation predicts a sharp peak in the computed SPL spectra at $f_{peak} = 840$ Hz, which is close to the frequency of the secondary spectral peak at 940 Hz in the measured combustion noise spectra. The mechanism causing this pronounced peak at $f_{peak} = 840$ Hz in the computed combustion noise spectra of the open LPHALS flame is elucidated in the next subsection.

From Figs. 17 and 18, it can be substantiated that the strongest acoustic sources of each type are typically confined within a region demarcated by $x \leq 40$ mm and $|y| < 40$ mm. Additionally, the physical phenomenon responsible for the manifestation of the sharp SPL peak at 840 Hz in the computed combustion noise spectra (discussed in Section 3.3), is also confined within the stream-wise region corresponding to 6 mm $\leq x \leq 26$ mm. Moreover, the axial and radial lengths of the LPHALS flame measured in the experiment, using the same definition of the flame boundary as that in Fig. 16 (i.e., 20% of the maximum mean value of OH* chemiluminescence intensity), are 28.1 mm and 56.8 mm, respectively. Now, the acoustic wavelengths (calculated using the speed of sound in ambient air at 300 K) corresponding to the frequencies of interest in this study, viz. 500 Hz and 940 Hz observed in the experiment, and 840 Hz predicted by the CAA simulation are 680 mm, 361.7 mm and 404.8 mm, respectively. Therefore, a comparison of the above-mentioned spatial extent or dimensions within which the strongest acoustic sources in the turbulent reacting flow-field are confined, and the axial and radial lengths of the LPHALS flame with the acoustic wavelengths of interest, reveals that the acoustic wavelengths are much larger. Hence, the current LPHALS flame can be considered acoustically compact.

3.3. Characteristics of radiated acoustic field

To investigate the cause of the peak in the computed SPL spectra at $f_{peak} = 840$ Hz, the spatial dependence of the correlation between heat release rate fluctuations and the far-field acoustic pressure perturbations p' are analysed. For this purpose, the stream-wise variation of the spectrum of the coherence $C_{q'_{rad}\,p'}(x, f)$ between the radially integrated heat release rate fluctuations at a given stream-wise location $q'_{rad}(x)$, and p' sampled at the far-field position of $(x, y) = (50$ mm, 180 mm), is shown in Fig. 23. It can be seen that there are strong correlations between $q'_{rad}(x)$ and p' around 840 Hz at several stream-wise locations. However, two stream-wise regions of particular importance can be substantiated from Fig. 23, viz. 16 mm $\leq x \leq 26$ mm and $x < 16$ mm. First, the stream-wise region within 16 mm $\leq x \leq 26$ mm is considered, and the temporal variation of the instantaneous temperature distribution in the central $x - y$ plane, obtained from the LES is examined in Fig. 24. From these instantaneous temperature distributions that are extracted over a time period of $T_p = 1/f_{peak}$ (i.e., $T_p = 1/840$ s), the generation of vortical flame structures is detected in the shear layers, i.e., within the region denoted by the yellow square in the temperature distributions shown in Fig. 24. Such vortical flame structures are found to shed consistently in this shear layer region over every cycle of duration $T_p = 1/840$ s, which indicates that there may be periodic interactions between the turbulent flow structures and the flame. Hence, if these vortical flame structures are indeed generated periodically, they are bound to produce local
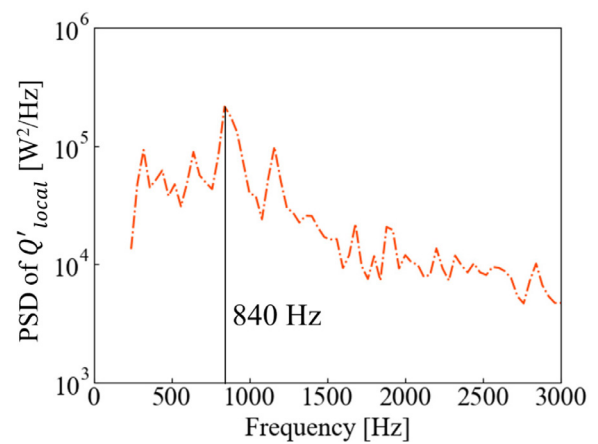

Fig. 25. Power spectral density (PSD) of local heat release rate fluctuations Q'_{local} occurring in the region indicated by the yellow square in Fig. 24, obtained from LES.
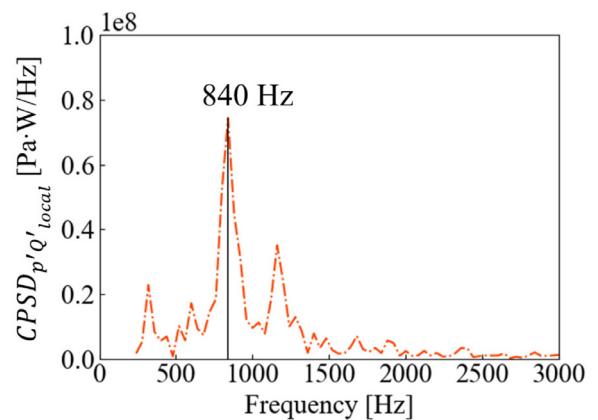

Fig. 26. Cross power spectral density $CPSD_{p'Q'_{local}}$ between the acoustic pressure perturbations p' computed at $(x, y) = (50$ mm, 180 mm), and the local heat release rate fluctuation Q'_{local} occurring in the region indicated by the yellow square in Fig. 24.

flame front deformations, which will consequently result in local heat release rate fluctuations at a specific frequency.

Therefore, the spectral characteristics of the local heat release rate fluctuations occurring in the shear layer region denoted by the yellow square in Fig. 24 are analysed next. Figure 25 depicts the power spectral density (PSD) of the local heat release rate fluctuations occurring within the region denoted by the yellow square. It is observed that the local heat release rate fluctuation spectrum also contains a pronounced (and the strongest) peak at 840 Hz, which seems to be consistent with the frequency f_{peak} of the sharp peak seen in the computed combustion noise spectra in Fig. 21. Furthermore, as evident from Fig. 21, the sharp SPL peak at 840 Hz appears in the computed noise spectra regardless of the observer position. Hence, to confirm whether a possible physical correlation exists between the local heat release rate fluctuations and direct combustion noise (i.e., acoustic pressure perturbations) at 840 Hz, the cross power spectral density (CPSD) between the acoustic pressure perturbation p' signal sampled at $(x, y) = (50$ mm, 180 mm) [the same position as that in Fig. 21(a)], and the local heat release rate fluctuations Q'_{local} (occurring in the region denoted by the yellow square in Fig. 24) is examined in Fig. 26. A pronounced sharp peak at 840 Hz with the highest amplitude is observed in the cross power spectrum as well, suggesting a direct and strong physical correlation between Q'_{local} and p' (i.e., direct combustion noise) at 840 Hz. Therefore, it can be confirmed that the peak in the combustion noise spectra at 840 Hz is caused by the intense
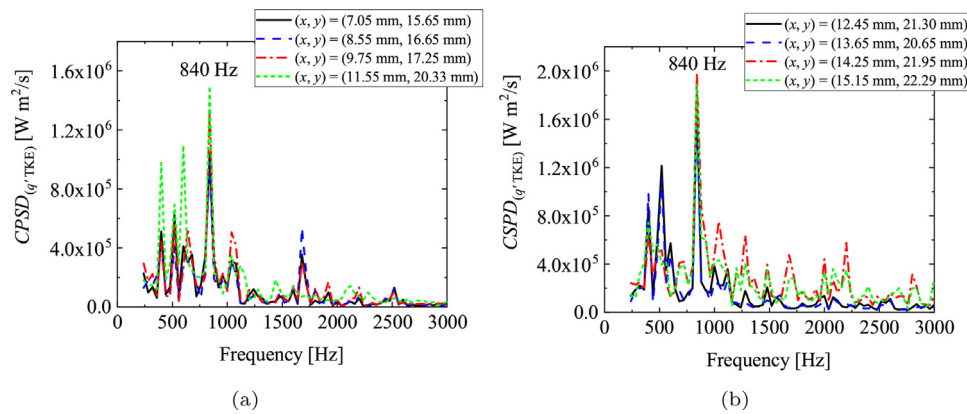
Fig. 27. Cross power spectral density $CPSD_{(q'\,\text{TKE})}$ between the heat release rate fluctuation $q'(x, y)$ and the turbulent kinetic energy TKE(x, y) at various positions along the flame front, in the shear layers for $x < 16$ mm.

local heat release rate fluctuations resulting from the periodically generated vortical flame structures in the shear layer region within 16 mm $\leq x \leq$ 26 mm. Such vortical flame structures arise due to the interaction between the flame and the vortices produced in the shear layers. The same mechanism was responsible for the secondary peak at 940 Hz in the measured combustion noise spectra in Shoji et al.'s work [21].

Contrary to the emergence of vortical flame structures in the shear layers of the stream-wise region within 16 mm $\leq x \leq$ 26 mm (see Fig. 24), such vortical flame structures are not apparent in the stream-wise region corresponding to $x < 16$ mm in the instantaneous temperature distributions shown in Fig. 24. However, based on the stream-wise variation of the spectrum of coherence $C_{q'_{rad}\,p'}(x, f)$ illustrated in Fig. 23, it was substantiated that there exist strong physical correlations between $q'_{rad}(x)$ and the far-field acoustic pressure perturbations p' around 840 Hz, even in the stream-wise region corresponding to $x < 16$ mm. Hence, even though vortical flame structures are not detected in this region, it is still possible that interactions between the flow turbulence and the flame front occur in the shear layers at stream-wise locations corresponding to $x < 16$ mm, which lead to the strong correlations between $q'_{rad}(x)$ and p' at 840 Hz. To confirm this hypothesis, the CPSD between the heat release rate fluctuations $q'(x, y)$ and the turbulent kinetic energy TKE(x, y), denoted by $CPSD_{(q'\,\text{TKE})}$, is computed at various positions (x, y) along the flame front, in the shear layers for $x < 16$ mm, and analysed in Fig. 27. The plots of $CPSD_{(q'\,\text{TKE})}$ depicted in Fig. 27, contain the highest amplitude pronounced sharp peak at 840 Hz for all positions along the flame front, indicating a direct and strong physical correlation between the heat release rate fluctuations and the flow field turbulence. Thus, the turbulence induced heat release rate fluctuations generated in the shear layers of the stream-wise region corresponding to $x < 16$ mm, are also responsible for the manifestation of the pronounced SPL peak at 840 Hz in the computed combustion noise spectra.

Results of the CAA simulation cases, i.e., case1, case2 and case3 (see Table 1) are analysed next, to investigate the impact of acoustic source terms $q_{e,rf}$ and $\boldsymbol{q}_{m,rf}$ on the acoustic field radiated by the open LPHALS flame. Specifically, the acoustic fields simulated in these three cases are analysed in terms of their spectral content and directivity characteristics. A separate CAA simulation considering only the acoustic source term $q_{c,rf}$ was deemed unnecessary, because this source term was found to be the weakest (see Section 3.2), and hence its contribution to the acoustic field will be negligible in comparison to those of $q_{e,rf}$ and $\boldsymbol{q}_{m,rf}$ [25,38]. SPL spectra computed at six observer positions indicated by the red circular points in Fig. 22, are compared among the CAA simula-

tions of case1, case2 and case3 in Fig. 28. The positions chosen for this analysis are at a fixed radial distance of $y = 180$ mm from the burner axis, and at six different streamwise x locations from the burner exit. In Fig. 28(a)–(c), it can be seen that the SPLs predicted by case1 (which considers all three acoustic source terms of the APE-RF system, viz. $q_{e,rf}$, $\boldsymbol{q}_{m,rf}$ and $q_{c,rf}$) and case2 (which considers only $q_{e,rf}$) are nearly identical across all frequencies. Additionally, in Fig. 28(d)–(f), it is observed that the SPLs predicted by case2 are only slightly lower than those predicted by case1 for frequencies below 1500 Hz. Furthermore, the SPL spectra obtained from case3 (which considers only the acoustic source term $\boldsymbol{q}_{m,rf}$) for all six positions, show that the SPLs are lower than those of case1 and case2 across all frequencies. This is because the source term $\boldsymbol{q}_{m,rf}$ was found to be 3 orders of magnitude smaller than $q_{e,rf}$ (see Figs. 18 and 17). Therefore, the results of case1, case2 and case3 for the computed SPL spectra in Fig. 28, suggest that the dominant contribution to the total SPL comes from the acoustic source term $q_{e,rf}$, while the contribution from the source term $q_{c,rf}$ to the total SPL is negligible across all frequencies. Moreover, noticeable attenuation of SPLs in the higher frequency range is observed in the noise spectra of all three CAA simulation cases, especially for the positions shown in Fig. 28(e) (SPL attenuation occurs for frequencies greater than 2000 Hz) and Fig. 28(f) (SPL reduction occurs for frequencies greater than 1500 Hz). These positions correspond to the farther downstream x locations from the burner exit (i.e., $x = 0$ mm). It is apparent that the farther the downstream location from the burner exit, the lower the noise radiation angle θ to the burner axis (described later), and the greater the reduction in SPL of the high-frequency noise emissions. This phenomenon is examined further by analysing the directivity behaviour of the radiated acoustic field in all three CAA simulation cases.

For the directivity evaluations, sound pressure levels at several specific frequencies are computed at various observer positions situated on a circular arc of radius $R = 360$ mm in the central $x - y$ plane, as depicted in Fig. 22. The center of this directivity evaluation arc is denoted by the yellow point P $[(x, y, z) = (20$ mm, 0 mm, 0 mm)] in Fig. 22, whose stream-wise location is chosen based on the results illustrated in Figs. 17(a) and 20. As evident from Fig. 17(a), the acoustic source term $q_{e,rf}$ is strong in the vicinity of $x = 20$ mm, and from the acoustic pressure perturbation field in the central $x - y$ plane shown in Fig. 20, excitation of strong pressure perturbations around $x = 20$ mm can be discerned. Therefore, the stream-wise location of the center of the directivity evaluation arc (yellow point P in Fig. 22) is chosen to be $x = 20$ mm. Each observer position on this circular arc corresponds to a certain noise radiation angle θ, which is defined as the angle between the x-axis (i.e., the burner axis) and a line segment joining the center
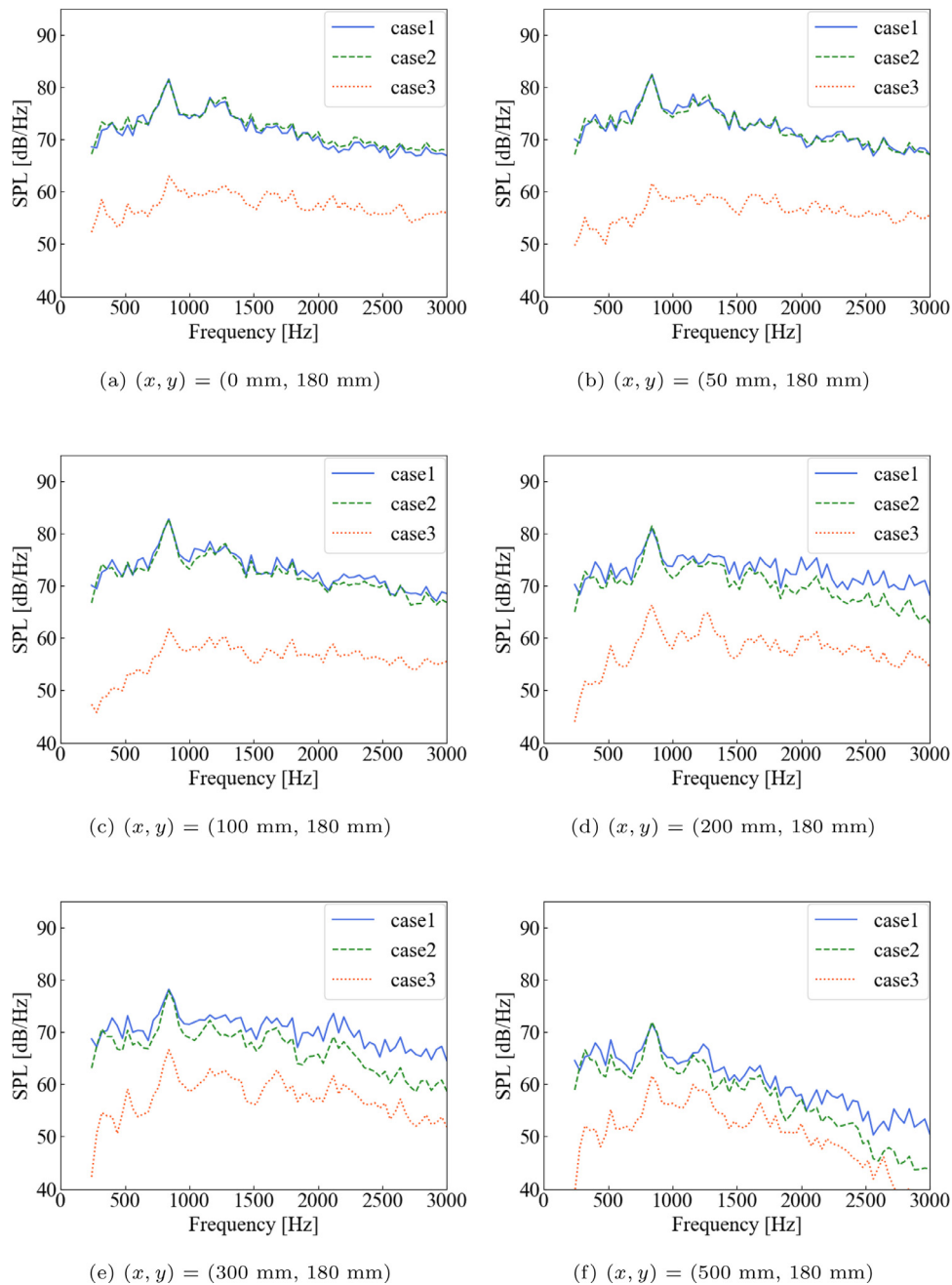
Fig. 28. Comparisons of sound pressure level (SPL) spectra among the CAA simulations of case1, case2 and case3, computed at six different positions indicated by the red circular points in Fig. 22. (For interpretation of the references to colour in this figure legend, the reader is referred to the web version of this article.)

of the circular arc (i.e, the yellow point P in Fig. 22) and an observer position on the arc (denoted by the yellow line in Fig. 22). Directivity plots are shown in Fig. 29 for all three CAA simulation cases for frequencies ranging from 400 Hz to 2640 Hz. Variations of the frequency-specific SPL with the radiation angle θ for frequencies below 1500 Hz, depicted in Fig. 29(a)–(d) show that the SPL in case2, which considers only the acoustic source term $q_{e,rf}$ of the pressure-density relation Eq. (9), remains nearly constant at all radiation angles except for $\theta < 20°$. This monopole-like directivity pattern generated by the source term $q_{e,rf}$ is attributed to the dominant source mechanism included in $q_{e,rf}$, viz. the unsteady heat release [56–58]. Similar directivity behaviour is observed in case1 (which considers all the acoustic source terms of the APE-RF system) for frequencies below 1500 Hz in Fig. 29(a)–(d).

On the contrary, from the directivity plots of frequency-specific SPL for frequencies above 1500 Hz, depicted in Fig. 29(e)–(h), it can be seen that the SPLs start to decrease for $\theta < 40°$ in all three CAA simulation cases. Such reductions in SPLs for $\theta < 40°$ at the higher frequencies, are caused by acoustic refraction effects due to spatially varying mean temperature within the turbulent flame [58,61]. To be more specific, mean temperature gradients in the flame will lead to gradients of the mean speed of sound $\hat{c}$, and the acoustic waves (produced by the sources) propagating in the downstream direction interact with these mean sound speed gradients to get refracted outwards, i.e., away from the flame/burner axis. Consequently, as evident from Fig. 29(e) - 29(h), the preferred direction of noise emissions at higher frequencies in case1 and case2 is $\theta \approx 40°$. Such deviations from the isotropic/monopole di-
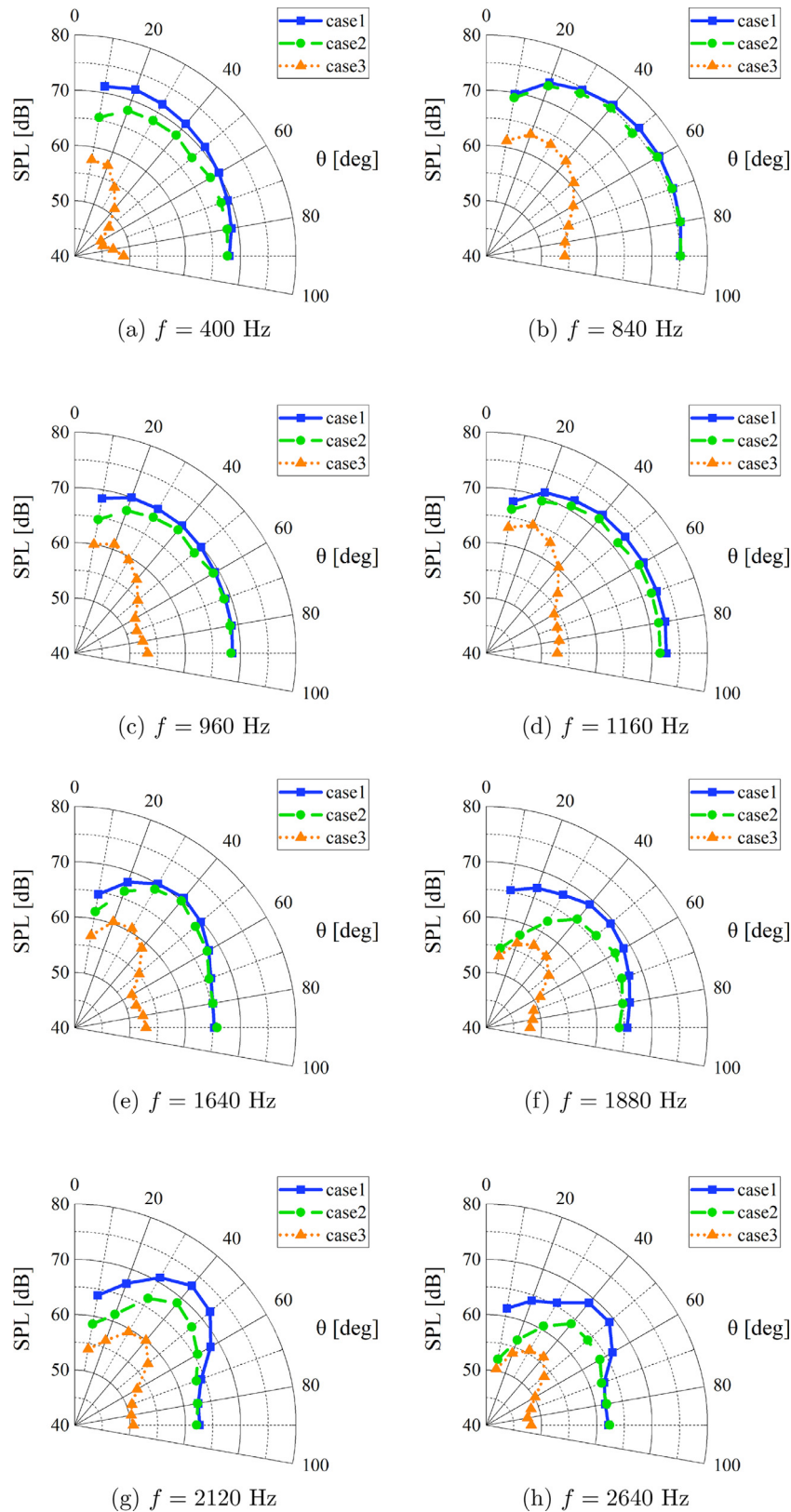
Fig. 29. Frequency-specific sound pressure level (SPL) computed at various positions on a circular arc of radius $R = 360$ mm in the $x - y$ plane ($z = 0$ mm), whose center is located at the point $(x, y, z) = (20$ mm, 0 mm, 0 mm), as depicted in Fig. 22. Observer positions are placed on this circular arc at an increment of $10°$, starting from a radiation angle $\theta = 10°$ up to $\theta = 90°$ to the burner axis. Results are compared among all three CAA simulation cases.

rectivity pattern arising from the aforementioned refraction effects due to mean sound speed gradients in the flame, have been studied extensively via experiments [11,58,61] and numerical simulations [13,38,62]. Moreover, it can also be observed that the higher the noise emission frequency, the more susceptible it is to the refraction effects, which is evidenced by the stronger attenuation of its SPL. Hence, attenuation of the high-frequency noise emissions observed in Fig. 28(e) and (f) for the far downstream positions (which correspond to radiation angles $\theta < 40°$), can be attributed to the aforementioned acoustic refraction effects.

Next, focussing on the results of case3 (which considers only the acoustic source term $\boldsymbol{q}_{m,rf}$ of the perturbation velocity Eq. (8)) in Fig. 29, it is evident from the directivity patterns that a strong directionality exists at all frequencies, contrary to case1 and case2. For frequencies below 1500 Hz, i.e, in Fig. 29(a)–(d), the preferred noise radiation direction is $\theta \approx 20°$. However, at frequencies above 1500 Hz, the noise directivity shifts to $\theta \approx 30°$ as shown in Fig. 29(e) and (f), and to $\theta \approx 40°$ as shown in Fig. 29(g) and (h). This shift in the preferred noise radiation direction is also caused by the acoustic refraction effects, and once again suggests that the influence of these refraction effects on the directivity behaviour becomes stronger with increasing noise emission frequency. Additionally, the noise directivity patterns observed in case3 are an indication of the inherent non-isotropic noise radiation characteristic of the source term $\boldsymbol{q}_{m,rf}$. In order to understand the strong noise directivity generated by the source term $\boldsymbol{q}_{m,rf}$, a detailed investigation of the directivity behaviours of the different source mechanisms contained in it [see Eq. (11)] would have to be performed. However, for such an investigation, additional CAA simulations to evaluate the individual contribution of each source mechanism in $\boldsymbol{q}_{m,rf}$ to the radiated non-isotropic acoustic field would have to be carried out. Such an analysis is beyond the scope of this paper and will be conducted in a future study.

4. Conclusions

Direct combustion noise generated by an open lean-premixed H_2/air low-swirl (LPHALS) turbulent flame was investigated using the hybrid LES/APE-RF framework. Acoustic field radiated by this flame was predicted by solving the system of Acoustic Perturbation Equations for Reacting Flows (APE-RF) in the CAA simulation. LES results for the flow-field velocity distributions and statistics, flame structure and lift-off height showed an overall favourable agreement with experimental data. SPL spectra obtained from the CAA simulation was unable to capture the first pronounced peak at 500 Hz that was observed in the measured combustion noise spectra. This discrepancy was attributed to the inflow boundary conditions for the turbulent velocity field applied at the burner exit in the LES, which did not exactly match with those in the experiment. The reason for this was the lack of the complex Low-Swirl Burner (LSB) geometry situated upstream of the burner exit in the LES. Consequently, the LES was unable to accurately predict the heat release rate fluctuations, which are the dominant source mechanism of direct combustion noise. However, the computed combustion noise spectra possessed a pronounced peak at a frequency of 840 Hz, which was close to the frequency of the secondary peak (at 940 Hz) in the measured combustion noise spectra. Appearance of this peak in the combustion noise spectra was attributed to the intense local heat release rate fluctuations in the shear layers. These heat release rate fluctuations induced by the periodic interactions of the turbulent flow structures with the flame front, were mainly confined in the shear layers of the stream-wise region within 6 mm $\leq x \leq$ 26 mm.

Influence of the acoustic source terms on the radiated acoustic field was investigated by analysing the spectral content and directivity of the noise generated by them. Three CAA simulations,

each considering different acoustic source terms were performed. Results showed that the source term of the pressure-density relation, i.e., $q_{e,rf}$, had the dominant contribution to the acoustic field generated by the open LPHALS flame, and the source term of the perturbation density equation, i.e, $q_{c,rf}$, had negligible contribution to the acoustic field. Additionally, SPLs generated by the source term of the perturbation velocity equation, i.e., $\boldsymbol{q}_{m,rf}$, were lower than those generated by $q_{e,rf}$. Attenuation of the SPLs at higher frequencies (i.e., frequencies greater than 1500 Hz) was observed for the farther downstream positions, which correspond to noise radiation angles with respect to the burner axis of less than 40°. These reductions in SPLs were attributed to the acoustic refraction effects caused by mean sound speed gradients in the flame (arising from spatially varying mean temperature in the flame). Inspection of the directivity characteristics of the radiated acoustic field at several specific frequencies revealed that, the source term $q_{e,rf}$ generates a monopole/isotropic directivity pattern for frequencies below 1500 Hz, but for the higher frequencies, its directivity behaviour deviates from the monopole character and exhibits a preferred noise radiation direction of around 40° to the burner axis, which was caused by the above-mentioned acoustic refraction effects. Similar noise directivity behaviour was observed in the CAA simulation which considered all three acoustic source terms of the APE-RF system (i.e., $q_{e,rf}$, $\boldsymbol{q}_{m,rf}$ and $q_{c,rf}$). Furthermore, directivity patterns produced by the source term $\boldsymbol{q}_{m,rf}$ showed strong directionality at all frequencies. The preferred noise radiation direction varied from 20° to the burner axis for frequencies below 1500Hz, up to 40° to the burner axis with increasing noise emission frequency in the higher frequency range. Such a shift in the preferred noise radiation angle was also attributed to the acoustic refraction effects arising from the mean sound speed gradients in the flame. Thus, the applicability of the hybrid LES/APE-RF framework to simulate the direct combustion noise (with pronounced spectral peak) generated by the open LPHALS turbulent flame was demonstrated in this study. It was confirmed that the hybrid LES/APE-RF framework can predict the important characteristics of direct combustion noise radiated by the open LPHALS flame.

Declaration of Competing Interest

The authors declare that they have no known competing financial interests or personal relationships that could have appeared to influence the work reported in this paper.

Acknowledgments

References

[1] R. Sankaran, E.R. Hawkes, J.H. Chen, T. Lu, C.K. Law, Direct numerical simulations of turbulent lean premixed combustion, J. Phys. Conf. Ser. 46 (2006) 38–42.

[2] A.P. Dowling, S.R. Stow, Acoustic analysis of gas turbine combustors, J. Propul. Power 19 (2003) 751–764.

[3] Y. Liu, A.P. Dowling, N. Swaminathan, R. Morvant, M.A. Macquisten, L.F. Caracciolo, Prediction of combustion noise for an aeroengine combustor, J. Propul. Power 30 (2013) 114–122.

[4] S. Candel, Combustion dynamics and control: progress and challenges, Proc. Combust. Inst. 29 (2002) 1–28.

[5] A.L. Pillai, J. Nagao, R. Awane, R. Kurose, Influences of liquid fuel atomization and flow rate fluctuations on spray combustion instabilities in a backward-facing step combustor, Combust. Flame 220 (2020) 337–356.

[6] W.C. Strahle, Combustion noise, Prog. Energy Combust. Sci. 4 (1978) 157–176.

[7] S. Kotake, K. Takamoto, Combustion noise: effects of the shape and size of burner nozzle, J. Sound Vib. 112 (1987) 345–354.

[8] S. Kotake, K. Takamoto, Combustion noise: effects of velocity turbulence of unburned mixture, J. Sound Vib. 139 (1990) 9–20.

[9] R. Rajaram, T. Lieuwen, Acoustic radiation from turbulent premixed flames, J. Fluid Mech. 637 (2009) 357–385.

[10] S.A. Klein, J.B.W. Kok, Sound generation by turbulent non-premixed flames, Combust. Sci. Tech. 149 (1999) 267–295.

[11] K.K. Singh, S.H. Frankel, J.P. Gore, Study of spectral noise emissions from standard turbulent nonpremixed flames, AIAA J. 42 (2004) 931–936.

[12] M. Ihme, H. Pitsch, D. Bodony, Radiation of noise in turbulent non-premixed flames, Proc. Combust. Inst. 32 (2009) 1545–1553.

[13] M. Ihme, H. Pitsch, On the generation of direct combustion noise in turbulent non-premixed flames, Int. J. Aeroacoust. 11 (2012) 25–78.

[14] M. Ihme, Combustion and engine-core noise, Annu. Rev. Fluid Mech. 49 (1) (2017) 277–310.

[15] J.E. Ffowcs Williams, M.S. Howe, The generation of sound by density inhomogeneities in low mach number nozzle flows, J. Fluid Mech. 70 (1975) 605–622.

[16] F.E. Marble, S. Candel, Acoustic disturbance from gas non-uniformities convected through a nozzle, J. Sound Vib. 55 (1977) 225–243.

[17] M.S. Howe, Indirect combustion noise, J. Fluid Mech. 659 (2010) 267–288.

[18] C. Shao, K. Maeda, M. Ihme, Analysis of core-noise contributions in a realistic gas-turbine combustor operated near lean blow-out, Proc. Combust. Inst. 38 (4) (2021) 6203–6211.

[19] C. Shao, D. Brouzet, N. Rock, M. Ihme, Parametric analysis of core-noise from a realistic gas-turbine combustor for cruise and take-off conditions, Appl. Energy Combust. Sci. 9 (2022) 100045.

[20] T. Schuller, D. Durox, S. Candel, Self-induced combustion oscillations of laminar premixed flames stabilized on annular burners, Combust. Flame 135 (2003) 525–537.

[21] T. Shoji, Y. Iwasaki, K. Kodai, S. Yoshida, S. Tachibana, T. Yokomori, Effects of flame behaviors on combustion noise from lean-premixed hydrogen low-swirl flames, AIAA J. 58 (10) (2020) 4505–4521.

[22] A.L. Pillai, R. Kurose, Numerical investigation of combustion noise in an open turbulent spray flame, Appl. Acoust. 133 (2018) 16–27.

[23] S. Schlimpert, S.R. Koh, K. Pausch, M. Meinke, W. Schröder, Analysis of combustion noise of a turbulent premixed slot jet flame, Combust. Flame 175 (2017) 292–306.

[24] K. Pausch, S. Herff, F. Zhang, H. Bockhorn, W. Schröder, Noise sources of lean premixed flames, Flow Turbul. Combust. 103 (2019) 773–796.

[25] T.P. Bui, W. Schröder, M. Meinke, Numerical analysis of the acoustic field of reacting flows via acoustic perturbation equations, Comput. Fluids 37 (2008) 1157–1169.

[26] A.L. Pillai, R. Kurose, Combustion noise analysis of a turbulent spray flame using a hybrid DNS/APE-RF approach, Combust. Flame 200 (2019) 168–191.

[27] K. Pausch, S. Herff, W. Schröder, Noise sources of an unconfined and a confined swirl burner, J. Sound Vib. 475 (2020) 115293.

[28] J.V. Oijen, L.D. Goey, Modelling of premixed laminar flames using flamelet-generated manifolds, Combust. Sci. Technol. 161 (2000) 113–137.

[29] P. Moin, K. Squires, W. Cabot, S. Lee, A dynamic subgrid-scale model for compressible turbulence and scalar transport, Phys. Fluids 3 (1991) 2746–2757.

[30] D.K. Lilly, A proposed modification of the Germano subgrid-scale closure method, Phys. Fluids 4 (3) (1992) 633–635.

[31] T. Honzawa, R. Kai, A. Okada, A. Valera-Medina, P.J. Bowen, R. Kurose, Predictions of NO and CO emissions in ammonia/methane/air combustion by LES using a non-adiabatic flamelet generated manifold, Energy 186 (2019) 115771.

[32] M. Chrigui, J. Gounder, A. Sadiki, A.R. Masri, J. Janicka, Partially premixed reacting acetone spray using LES and FGM tabulated chemistry, Combust. Flame 159 (2012) 2718–2741.

[33] J.A. Miller, C.T. Bowman, Mechanism and modeling of nitrogen chemistry in combustion, Prog. Energy Combust. Sci. 15 (1989) 287–338.

[34] M. Ó Conaire, H.J. Curran, J.M. Simmie, W.J. Pitz, C.K. Westbrook, A comprehensive modeling study of hydrogen oxidation, Int. J. Chem. Kinet. 36 (2004) 603–622.

[35] F. Egolfopoulos, C. Law, An experimental and computational study of the burning rates of ultra-lean to moderately-rich H2/O2/N2 laminar flames with pressure variations, Symp. (Int.) Combust. 23 (1) (1991) 333–340.

[36] N. Lamoureux, N. Djebaïli-Chaumeix, C.-E. Paillard, Laminar flame velocity determination for H2–air–He–CO2 mixtures using the spherical bomb method, Exp. Therm. Fluid Sci. 27 (4) (2003) 385–393.

[37] H. Pitsch, FlameMaster: A C++ computer program for 0D combustion and 1D laminar flame calculations, 1998.

[38] T.P. Bui, M. Ihme, W. Schröder, H. Pitsch, Analysis of different sound source formulations to simulate combustion generated noise using a hybrid LES/APE-RF method, Int. J. Aeroacoustics 8 (2009) 95–124.

[39] D.G. Crighton, A.P. Dowling, J.E. Ffowcs Williams, M. Heckl, F.G. Leppington, Modern methods in analytical acoustics, Springer, 1992.

[40] T.P. Bui, W. Schröder, M. Meinke, Acoustic perturbation equations for reacting flows to compute combustion noise, Int. J. Aeroacoust. 6 (2007) 335–355.

[41] H. Moriai, R. Kurose, H. Watanabe, Y. Yano, F. Akamatsu, S. Komori, Large-eddy simulation of turbulent spray combustion in a subscale aircraft jet engine combustor–predictions of NO and soot concentrations, J. Eng. Gas Turbines Power 135 (9) (2013) 091503.

[42] S. Tachibana, K. Saito, T. Yamamoto, M. Makida, T. Kitano, R. Kurose, Experimental and numerical investigation of thermo-acoustic instability in a liquid–fuel aero-engine combustor at elevated pressure: validity of large-eddy simulation of spray combustion, Combust. Flame 162 (6) (2015) 2621–2637.

[43] M. Klein, A. Sadiki, J. Janicka, A digital filter based generation of inflow data for spatially developing direct numerical or large eddy simulations, J. Comput. Phys. 186 (2003) 652–665.

[44] A.M. Kempf, S. Wysocki, M. Pettit, An efficient, parallel low-storage implementation of Klein's turbulence generator for LES and DNS, Comput. Fluids 60 (2012) 58–60.

[45] C. Bogey, C. Bailly, Three-dimensional non-reflective boundary conditions for acoustic simulations: far field formulation and validation test cases, Acta. Acust. united Acust. 88 (2002) 463–471.

[46] About in-house code FK³, (visited on 12/05/2021), http://www.tse.me.kyoto-u.ac.jp/members/kurose/link_e.php.

[47] V. Moureau, C. Bérat, H. Pitsch, An efficient semi-implicit compressible solver for large-eddy simulations, J. Comput. Phys. 226 (2) (2007) 1256–1270.

[48] Y. Morinishi, T. Lund, O. Vasilyev, P. Moin, Fully conservative higher order finite difference schemes for incompressible flow, J. Comput. Phys. 143 (1998) 90–124.

[49] G.-S. Jiang, C.-W. Shu, Efficient implementation of weighted ENO schemes, J. Comput. Phys. 126 (1996) 202–228.

[50] R.J. Kee, D.-L. Graham, J. Warnatz, M.E. Coltrin, J.A. Miller, A Fortran computer code package for the evaluation of gas-phase, multicomponent transport properties, SANDIA Report No. SAND86-8246, Sandia National Laboratories, Albuquerque NM, Livermore CA, 1986.

[51] R.J. Kee, F.M. Rupley, J.A. Miller, Chemkin-II: A FORTRAN chemical kinetics package for the analysis of gas-phase chemical kinetics, SANDIA Report No. SAND89-8009B, Sandia National Laboratories, Albuquerque NM, Livermore CA, 1989.

[52] C.K.W. Tam, J.C. Webb, Dispersion-relation-preserving finite difference schemes for computational acoustics, J. Comput. Phys. 107 (1993) 262–281.

[53] F.Q. Hu, M.Y. Hussaini, J.L. Manthey, Low-dissipation and low-dispersion Runge-Kutta schemes for computational acoustics, J. Comput. Phys. 124 (1996) 177–191.

[54] C.K.W. Tam, H. Shen, Direct computation of nonlinear acoustic pulses using high order finite difference schemes, AIAA Paper 93-4325, 1993.

[55] R.K. Cheng, D.T. Yegian, M.M. Miyasato, G.S. Samuelsen, C.E. Benson, R. Pellizzari, P. Loftus, Scaling and development of low-swirl burners for low-emission furnaces and boilers, Proc. Combust. Inst. 28 (1) (2000) 1305–1313.

[56] T.J.B. Smith, J.K. Kilham, Noise generation by open turbulent flames, J. Acoust. Soc. Am. 35 (1963) 715–724.

[57] B.N. Shivashankara, W.C. Strahle, J.C. Handley, Combustion noise radiation by open turbulent flames, AIAA Paper 1973-1025, 1973.

[58] W.C. Strahle, Some results in combustion generated noise, J. Sound Vib. 23 (1972) 113–125.

[59] W.C. Strahle, B.N. Shivashankara, A rational correlation of combustion noise results from open turbulent premixed flames, Proc. Combust. Inst. 15 (1975) 1379–1385.

[60] S. Herff, K. Pausch, H. Nawroth, S. Schlimpert, C. Paschereit, W. Schröder, Impact of burner plenum acoustics on the sound emission of a turbulent lean premixed open flame, Int. J. Spray Combust. Dyn. 12 (2020). 1756827720956906

[61] W.C. Strahle, Refraction, convection, and diffusion flame effects in combustion–generated noise, Proc. Combust. Inst. 14 (1) (1973) 527–535.

[62] T.P. Bui, W. Schröder, Acoustic wave refraction in open turbulent flames, Acta. Acust. united Acust. 95 (2009) 440–447.